
# NAVAL POSTGRADUATE SCHOOL

**MONTEREY, CALIFORNIA**

# THESIS

**CHARGE TRANSPORT STUDY OF INGAAS QWIPS**

by

Vu D. Hoang

June 2004

Thesis Advisor: Nancy M. Haegel
Co-Advisor: John Powers

**Approved for public release; distribution is unlimited**

THIS PAGE INTENTIONALLY LEFT BLANK

| REPORT DOCUMENTATION PAGE | | | Form Approved OMB No. 0704-0188 |
|---|---|---|---|
| Public reporting burden for this collection of information is estimated to average 1 hour per response, including the time for reviewing instruction, searching existing data sources, gathering and maintaining the data needed, and completing and reviewing the collection of information. Send comments regarding this burden estimate or any other aspect of this collection of information, including suggestions for reducing this burden, to Washington headquarters Services, Directorate for Information Operations and Reports, 1215 Jefferson Davis Highway, Suite 1204, Arlington, VA 22202-4302, and to the Office of Management and Budget, Paperwork Reduction Project (0704-0188) Washington DC 20503. | | | |
| **1. AGENCY USE ONLY** ***(Leave blank)*** | **2. REPORT DATE** June 2004 | **3. REPORT TYPE AND DATES COVERED** Master's Thesis | |
| **4. TITLE AND SUBTITLE**: Charge Transport Study of InGaAs Two-color QWIPs. | | | **5. FUNDING NUMBERS** |
| **6. AUTHOR: Vu Dinh Hoang** | | | |
| **7. PERFORMING ORGANIZATION NAME(S) AND ADDRESS(ES)** Naval Postgraduate School Monterey, CA 93943-5000 | | | **8. PERFORMING ORGANIZATION REPORT NUMBER** |
| **9. SPONSORING /MONITORING AGENCY NAME(S) AND ADDRESS(ES)** N/A | | | **10. SPONSORING/MONITORING AGENCY REPORT NUMBER** |
| **11. SUPPLEMENTARY NOTES** The views expressed in this thesis are those of the author and do not reflect the official policy or position of the Department of Defense or the U.S. Government. | | | |
| **12a. DISTRIBUTION / AVAILABILITY STATEMENT** Approved for public release; distribution is unlimited | | | **12b. DISTRIBUTION CODE** |


**13. ABSTRACT (maximum 200 words)**

In this thesis, a series of experiments were performed to characterize the material properties of InGaAs/GaAs for use in a two-color quantum-well IR photodetector (QWIP) design. Results from room temperature studies using cathodoluminescence and photoluminescence indicated light emission at 858 nm and 1019 nm from GaAs and InGaAs, respectively. Using a direct transport imaging technique, an edge dislocation pattern was observed and shown to be confined to the InGaAs layer of the material. A dislocation density measurement was performed and was shown to be less than 2000 lines/cm. Quantitative intensity level measurements indicated fluctuation in the region of dislocations to be less than 30% of the signal to background level. Finally, a spot mode study using the direct transport imaging method was performed to evaluate the feasibility of using this technique for contact-less diffusion length measurements.


| **14. SUBJECT TERMS** dual-band IR detector, InGaAs/GaAs two-color QWIPs, Direct Transport Imaging, contact-less diffusion measurements | | | **15. NUMBER OF PAGES** 73 |
|---|---|---|---|
| | | | **16. PRICE CODE** |
| **17. SECURITY CLASSIFICATION OF REPORT** Unclassified | **18. SECURITY CLASSIFICATION OF THIS PAGE** Unclassified | **19. SECURITY CLASSIFICATION OF ABSTRACT** Unclassified | **20. LIMITATION OF ABSTRACT** UL |

NSN 7540-01-280-5500 Standard Form 298 (Rev. 2-89)
Prescribed by ANSI Std. 239-18

THIS PAGE INTENTIONALLY LEFT BLANK

**Approved for public release; distribution is unlimited**

# CHARGE TRANSPORT STUDY OF InGaAs TWO COLOR QWIPs

Vu D. Hoang
DoD Civilian, Department of Air Force
B.S., University of Nevada, Reno, 1989

Submitted in partial fulfillment of the
requirements for the degree of

**MASTER OF SCIENCE IN ELECTRICAL ENGINEERING**

**NAVAL POSTGRADUATE SCHOOL**
**June 2004**

Author: Vu Dinh Hoang

Approved by: Prof. Nancy M. Haegel
Thesis Advisor

Prof. John P. Powers
Co-Advisor

John P. Powers
Chairman, Department of Electrical and Computer Engineering

THIS PAGE INTENTIONALLY LEFT BLANK

# ABSTRACT

In this thesis, a series of experiments were performed to characterize the material properties of InGaAs/GaAs for use in a two-color quantum-well IR photodetector (QWIP) design. Results from room temperature studies using cathodoluminescence and photoluminescence indicated light emission at 858 nm and 1019 nm from GaAs and InGaAs, respectively. Using a direct transport imaging technique, an edge dislocation pattern was observed and shown to be confined to the InGaAs layer of the material. A dislocation density measurement was performed and was shown to be less than 2000 lines/cm. Quantitative intensity level measurements indicated fluctuation in the region of dislocations to be less than 30% of the signal to background level. Finally, a spot mode study using the direct transport imaging method was performed to evaluate the feasibility of using this technique for contact-less diffusion length measurements.

THIS PAGE INTENTIONALLY LEFT BLANK

# TABLE OF CONTENTS

THIS PAGE INTENTIONALLY LEFT BLANK

# LIST OF FIGURES

# LIST OF TABLES

THIS PAGE INTENTIONALLY LEFT BLANK

# ACKNOWLEDGMENTS

I would like to thank the EWE organization and the supporting staffs at HRD, Edwards AFB, CA, for giving me an opportunity to participate in this LTFT program at the Naval Postgraduate School in Monterey, CA. Being able to attend and complete this program had made an indelible mark in my personal life as well as my professional career.

I would like to thank Professor Gamani Karunasiri for providing all of the material samples used in this investigation. His ideas and suggestions were invaluable in the completion of this thesis.

I also like to thank Dr. Wu Junqiao at the Lawrence Berkeley National Laboratory for his assistance with the photoluminescence measurements.

I am forever indebted to my advisor, Professor Nancy Haegel, for her tireless efforts and insightful guidance from the initial study to the final write-up of this thesis. I was hesitant at first to choose a thesis topic where there were no guaranteed results, and she had convinced me to accept the challenge of "real world" research where "you don't know the answer".

I am very grateful to have Professor John Powers as my co-advisor for this thesis. His thorough reviews, both in term of scientific contents and formats made me aware of the high standard he demanded of all graduates of the ECE program at NPS.

Finally, I thank my wife and my daughter for all of their sacrifices during my entire time at NPS. I also acknowledge my mother who kept urging me to never stop learning and improving every single day.

THIS PAGE INTENTIONALLY LEFT BLANK

# EXECUTIVE SUMMARY

The concept of a dual-band quantum-well infrared photodetector or two-color QWIP using both the interband and intrasubband transitions arose from a need to detect IR energy at two different portions of the infrared band. Most laser target designators emit in the near IR band at the wavelength of 1.06 μm. The long-wave IR detectors in most thermal imaging IR devices, on the other hand, operate in the 8-12 μm band, respectively. Since the illumination energy is outside the spectral range of the detector, this sensor is blinded to the laser target designator's reflection. An alternative approach is to use the quantum-well methodology with InGaAs/GaAs material to design a dual-band detector where IR radiation from both the laser target designator and the thermal imaging IR can be sensed simultaneously.

A dual-band quantum well IR photodetector or QWIP was built and tested at NPS by Touse in 2003. During testing, the peak absorption in the NIR band was found to be lower than the specification of 1.06 μm and a recommendation was made to correct this deficiency. By increasing the concentration of indium in the InGaAs compound from the present value of 30% to a higher value, the principle investigator hoped to fix for the shortfall in the NIR band. Any change in material composition should be studied carefully, and the objective of this thesis was to perform material characterization study of the InGaAs compound in this dual-band quantum-well IR photodetector design.

Two of the most common experimental techniques to study light emission or absorption in a material are photoluminescence (PL) and cathodoluminescence (CL). Both of these experimental procedures were applied to this material and the results showed peak emission at 858 nm and 1019 nm. These values corresponded to the bandgap characteristic of GaAs and the quantum-well emission of InGaAs, respectively.

A new experimental method called direct transport imaging was also successfully applied to study material properties of InGaAs/GaAs. This technique uses a CCD camera in conjunction with an optical microscope to record the spatial information about charge carrier motion and recombination. Analysis using imaging data from this method showed

dislocation line patterns in the InGaAs layer due to lattice mismatch between indium and gallium atoms. Further studies were able to demonstrate that these dislocation misfits did not propagate upward to the cap layer of the device. Dislocation density was obtained for these patterns and their average value were measured to be about 2000 lines/cm. The intensity fluctuation within these dislocation patterns was found to be 30% of the signal to background level. These values showed that the material should be able to tolerate a higher concentration of Indium without significantly affecting the operation of the device.

Additional work performed showed possible application of the direct transport imaging technique in spot mode to measure the diffusion length of charges in a material without the need for application of contacts. This would allow the extraction of an important transport parameter (minority carrier lifetime) from an optical image. Initial results were encouraging but additional data and analysis methodology needs to be developed before conclusive data can be extracted for this application.

# I. INTRODUCTION

## A. IR DETECTION AND GENERATION TECHNOLOGY

Figure 1-1 illustrates the classification of the electromagnetic spectrum into spectral bands by wavelength $\lambda$, frequency $f$, or energy (in units of eV). Within the past few decades, we have dramatically expanded our ability to detect and generate radiation in spectral bands beyond the normal region of human vision (0.4–0.78 μm, Fig. 1-1). One of the spectral bands that has received a lot of attention is the infrared portion of the electromagnetic spectrum (1–1000 μm, Fig. 1-1). The ability to sense and manipulate signals in the infrared has enabled us to build remote control devices for TV, infrared cameras for astronomical and law enforcement purposes, laser transceivers for fiber-optic communications and medical diagnostic tools. More and more applications for this technology are being found everyday and well into the foreseeable future.

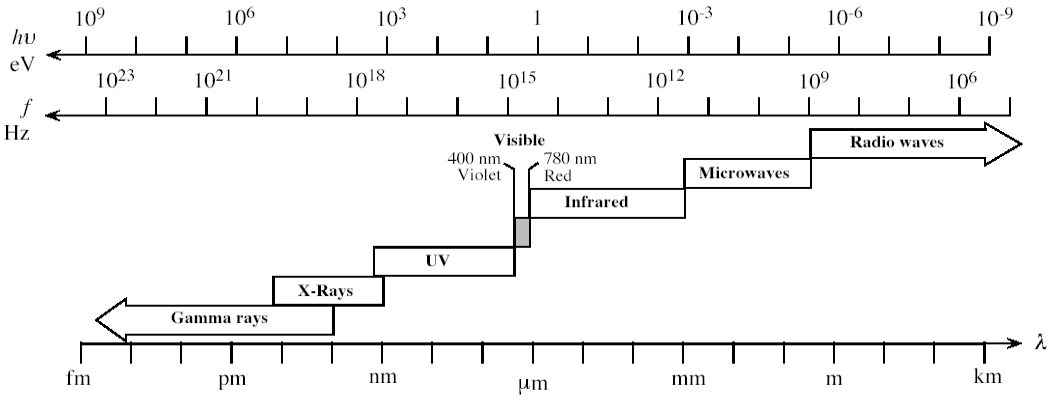


Fig. 1-1. The electromagnetic spectrum and the various bands designation. (From [10].)

One of the most important uses of infrared technology is in the area of battlefield surveillance and exploitation. In fact, infrared detectors such as the forward looking IR, or FLIR, and the night vision devices are allowing the US military to operate seamlessly from day into the night. At the same time, IR generation devices, such as laser target designators, have enabled us to strike most stationary targets with pinpoint accuracy. These

technological developments are the culmination of increased understanding in the area of solid-state physics, since they generally depend on semiconductor materials to either detect or generate the IR signals.

## B. TWO-COLOR IR DETECTOR TECHNOLOGY

The two-color IR detector is an attempt to mitigate the problem of using systems that emit and detect radiation at different wavelengths. Currently, most military battle-field IR surveillance detectors operate at the long-wave IR band (LWIR) of 8–12 μm. This is done to take advantage of an atmospheric transmissive window at these wave-lengths and the thermal emission of most objects at ambient temperature (~300K) in the absence of sunlight (night time). A room temperature object emitting as a blackbody ra-diation will have its peak emission at ~ 10 μm.

IR target designation, on the other hand, is done by directing a radiation source, such as a laser, at a target and viewing the reflected energy. Most laser target designators use the near IR band of 1.06 μm due to the availability of a laser devices and night vision goggle specifications. Therefore, the long-wave IR detection system and near-IR target designation technique are operating at two different portions of the IR regions. This means sensing of the laser reflection and the target thermal radiation would require two separate sensors/detectors. This adds cost, complexity, and additional signal processing requirements to the system. If we can build a detector with a capability to sense IR radia-tion at both near- and long-wave IR bands simultaneously, these problems can be elimi-nated. Our increased knowledge in solid-state physics of semiconductor materials has fi-nally allowed us to build such a device. Using the interband electron transition for sens-ing the laser designator radiation at 1.06 μm and a less energetic intersubband electron transition to detect thermal radiation, a dual band IR sensor can be fabricated. The con-cepts of interband and intersubband transition are explained in Chapter II.

A proof-of-concept two-color IR detector was built and tested at NPS in 2003 [1]. The device showed peak photoresponse at 0.8 μm and 10 μm, simultaneously. Although the design goal of 1.06 μm was not reached in the NIR band, the investigator claimed that

by changing the concentration of Indium in the InGaAs compound (currently at 10 and 30%), detections at 1.06 and 10.6 μm wavelength specifications should be achievable.

## C. PURPOSE OF THIS THESIS

The purpose of this thesis was to perform material characterization of two-color InGaAs/GaAs quantum-well IR photodetectors. This is done to investigate the effects of using InGaAs in a multiple quantum-well structure. Utilizing the scanning electron microscope laboratory in the Physics Department at NPS, cathodoluminescence (CL) studies were performed to measure the luminescence of the material under difference excitation conditions. Photoluminescence (PL) studies at Lawrence Berkeley National Laboratory were also carried out by the author to supplement results from CL. These data were used to determine the suitability of InGaAs/GaAs to operate in the NIR region.

A new experimental method called direct transport imaging was applied to study the effect of strain in the InGaAs layers of the quantum-well device. Previous studies have shown that building InGaAs layers on GaAs by means of molecular beam epitaxy will induced dislocation lines due to lattice mismatch. To optimize the design of this detector, material characterization needs to be performed on the effect of growing strained InGaAs layers on GaAs. As the stress induced due to lattice mismatching is unknown, once we have a clear understanding of the effect, this will help improve the detector's design and facilitate the building of second-generation devices.

## D. MILITARY RELEVANCE

One of the most important issues facing the military in the recent conflict was the problem of fratricide. This scenario could occur when crew has to determine the correct target while switching between different sensors. By integrating the detection of both IR bands into one sensor and combine the output, this will definitely help reducing the crew's workload and may help reduce the possibility of fratricide during close quarter engagement. In addition, increasing demands of multiple sensor systems has increased the need for ease of data fusion. This would be a direct result of the new detection technology described and studied in this thesis.

## E. THESIS OVERVIEW

Chapter I describes the current IR detection/generation technology and explains the military requirements for a two-color IR detection device. The need to optimize this two-color quantum-well photodetector design leads to the investigation of using InGaAs in GaAs quantum well structures, which is the objective of this thesis. The basics concept in quantum-well design is presented in Chapter II, to be followed by material characterization studies of InGaAs in Chapter III and IV. The conclusion of this study and important lessons learned are discussed in Chapter V.

# II. PHYSICS OF QWIPS

## A. BASICS OF QWIPS

Traditional IR photodetectors work by converting optical energy into an electrical signal. This conversion process starts when incident photons with energy greater than the bandgap of the detector material are absorbed, while less energetic photons pass through unabsorbed (Fig. 2-1). This bandgap energy forms the long wavelength detection limit for intrinsic detectors and can be expressed as follows:

$$E_g[\text{eV}] = 1.24/\lambda\ [\mu\text{m}] \tag{2.1}$$

where $E_g$ is the bandgap energy of the material (in eV) and $\lambda$ is the wavelength of incident photon (in micrometers).

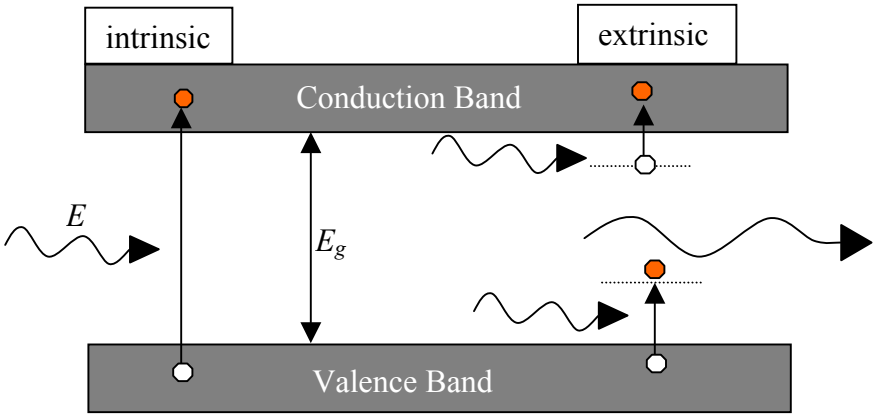


Fig. 2-1. Photon absorption in traditional IR detector. (After [2].)

When a photon of sufficient energy ($E > E_g$) is absorbed in the material, carriers are generated by either interband transitions (intrinsic) or by transitions involving forbidden-gap energy states (extrinsic). Intrinsic absorption, as seen on the left of Fig. 2-1, is characterized by electron excitation from the valence band (VB) to the conduction band (CB), also known as the fundamental absorption edge. On the other hand, extrinsic absorption relies on doped impurities to donate an electron (n-type) or to accept an electron (p-type) as a result of interaction with the incident photon. A visual interpretation of this phenomenon is shown on the right portion of Fig. 2-1. It is these two types of absorption that formed the cornerstone of IR detection technology for the past three decades.

Atmospheric absorption also played an important role in shaping the development of IR detector technology. Sharp absorption lines due to $H_2O$ vapor and other gases ($O_3$, $CO_2$) effectively divide the electromagnetic spectrum into several transmissive "windows" with very high absorptive regions in between. Most notable of these "windows" are the 3-5 ∝m and 8-12 ∝m bands. In military applications, these two bands are designated mid-IR (MWIR) and long-IR (LWIR), respectively. The LWIR band is of special interest since almost all objects at ambient temperature (300K) emit at this wavelength (~10 ∝m), as described by Wien's law:

$$\lambda_m[\mu\text{m}] = \frac{2896}{T[\text{K}]} \tag{2.2}$$

where $\lambda_m$ is the peak blackbody wavelength and $T$ is the temperature in Kelvin.

Military applications have great interest in detecting IR emission in this particular band. Unfortunately, it is very difficult to find materials that have energy bandgap corresponding to this wavelength: $E_g[\text{eV}] = 1.24/10[\mu\text{m}] = 0.124$ eV. HgCdTe and InAsSb are among the few small bandgap materials that have an electronic transition from VB to CB of around 0.1 eV. These materials suffer from a number of difficulties (material control, uniformity, yield) that greatly affect the device's performance and manufacturing cost. When placing these devices in an array to form an imaging sensor, these materials have high non-uniformity from one pixel to the next.

Quantum Well Infrared Photodetectors (QWIPs) represent a more recent approach to develop material suitable for LWIR detectors. This approach offers numerous benefits such as ease of manufacturing, lower cost, and improved array uniformity but the most important aspect is the ability to engineer the electrical and optical characteristics of the final product. References 5-9 provide an excellent overview of QWIP development.

The first quantum-well IR photodetector were built at AT&T Bell Labs in 1987 [9, 12]. A typical QWIP is formed by depositing layers of different bandgap materials next to one another by means of molecular beam epitaxy (MBE) or metal organic chemical vapor deposition (MOCVD). In controlling the thickness of the layer (well-width) and choosing the appropriate composition for materials in the layer (barrier-height), a region in the material that resembles a finite square well can be formed (Fig. 2-2.). This type of

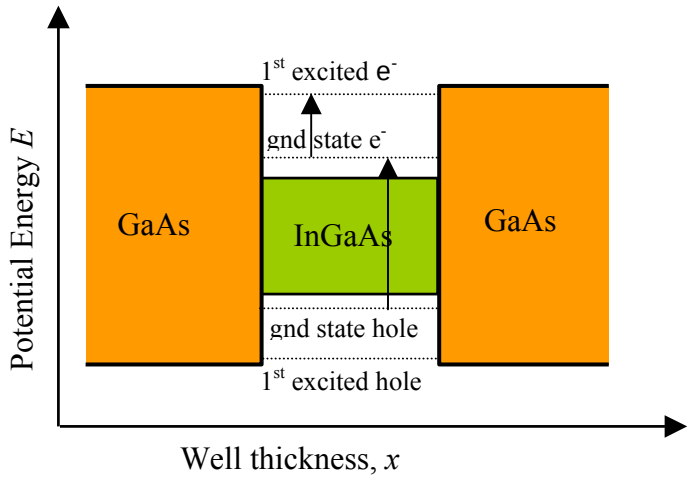


Fig. 2-2. Potential energy versus growth direction in a QWIP (After [1].)

structure is known as "the particle in a finite square well" problem and is commonly taught in elementary quantum mechanics. A square potential well is formed by embedding a small band gap material, InGaAs, between two large bandgap GaAs layers. The vertical axis of Fig. 2-2 denotes the bandgap energy levels of the materials forming the well while the horizontal arrow represents the thickness of layers. Viewed from the side, this structure resembles a square potential well. Solutions for this type of problem can be found by solving the Schrödinger's wave equation and applying the boundary conditions. Numerous elementary quantum mechanics textbooks [4, 5] have dealt with this topic extensively and only the final solutions are described here. We solve the following set of equations for the allowed energy states .

$$(1^{st}\text{class}) \qquad . \tan \; = \sqrt{\frac{mV_0L^2}{2\hbar^2} - .^{\;2}} \tag{2.3}$$

$$(2^{nd}\ \text{class}) \qquad -. \cot \; = \sqrt{\frac{mV_0L^2}{2\hbar^2} - .^{\;2}} \tag{2.4}$$

where . can be expressed as $. = \sqrt{mEL^2/2\hbar^2}$, $m$ is mass of electron, $V_0$ is the barrier-height, $L$ is the well-width, and $\hbar$ is Planck's constant divided by $2\pi$.

The important result from solving the set of transcendental equations above is that the potential energy difference at the InGaAs well's boundaries causes the formation of quantized or bounded energy states inside the well in the CB as well as VB. This is illus-

trated by a set of two dashed lines above the InGaAs region of Fig. 2-2 with each line represents a quantized energy level in the conduction band that an electron in the well can occupy. Similarly, the two dashed lines below the green region of Fig. 2-2 represent the discrete energy states for the holes in the valence band.

Another important result is that the energy levels and the number of states in a quantum well can be controlled by adjusting the device's parameters (barrier-height and well-width). In most cases, these parameters are carefully selected so that a well would hold only two confined states (a ground state and 1st excited state). As a result, electron transition is now possible between these bound states inside a quantum-well. Notice that since the electron transition is bound-to-bound (intersubband), the well region needs to be doped with either a donor impurity (n-type) or acceptor (p-type) for this scheme to work. As an example, if the well region is doped with donor atoms, the electron transition between the ground and the first excited state can occur for a photon with energy $h. = . E = E_{excited} - E_{ground}$, where $E_{excited}$ and $E_{ground}$ can be tuned using the barrier-height $V_0$ and the well-width $L$. Utilizing this methodology, the IR detector can be designed for detection of a specific wavelength, without the need to search for an intrinsic material with the correct bandgap. Current QWIPs can be tuned to cover a wide portion of the IR spectrum from 3 to 20 ∝m [7-9, 12].

## B. DESIGN OF A TWO COLOR QWIP

The two-color QWIP described here is an InGaAs/GaAs sample obtained from the work of Michael Touse in the Physics Department at NPS [1]. This device was fabricated to simultaneously detect IR radiation at two wavelengths, 1.04 and 10.4 ∝m. The energy band diagram for this device is shown in Fig. 2-3. The intraband transition (ground to 1st excited state) described in the section above would be used for detection in the thermal imaging 10-∝m region. The barrier-height and well-width design parameters need to be manipulated so that the potential energy of 1st excited state electron in the InGaAs region (E2 in Fig. 2-3) is equal to those of the GaAs region, also known as the barrier-height. This is done so that under external bias, the excited electrons from the In-

GaAs well could produce the necessary photocurrent without encountering any potential energy barriers at the GaAs interfaces.

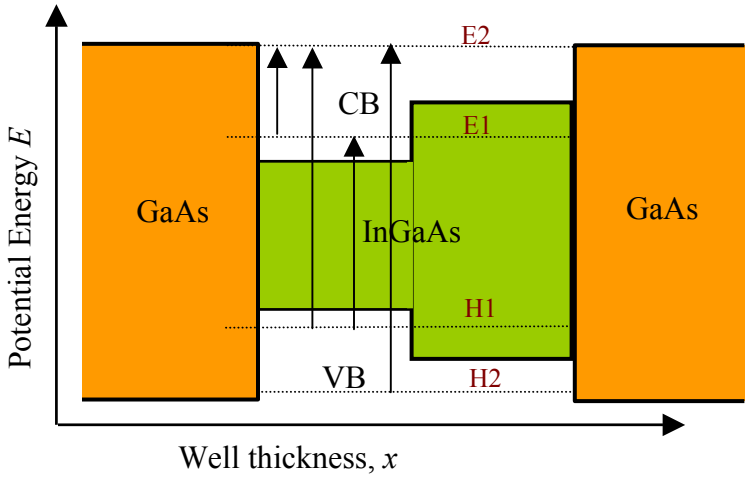


Fig. 2-3. Potential energy versus growth direction in an asymmetrical QWIP (After [1].)

However, to achieve 1.04-∝m detection, a more energetic interband transition such as those from VB to CB (H1 to E2 in Fig. 2-3.) would be needed. By adjusting the composition of indium in the ternary compound InGaAs, the bandgap energy can be modified according to the following bandgap energy expression,

$$\mathrm{Ga}_x\mathrm{In}_{1-x}\mathrm{As}\ [\mathrm{eV}] = 0.36 + 1.064x \tag{2.5}$$

where $x$ is the percentage of elemental Ga composition ranging from 1% to 99%. Thus, it is possible to engineer a bandgap energy separation such that absorption for 1.04 μm is achievable.

An additional constraint on a band-to-band transition rate, $W$, is defined by Fermi's golden rule for time-dependent perturbation theory [4, 5],

$$W = \frac{2\pi}{\hbar}\sum_{i,f}\left|\left\langle . \ _f \left|V_p\right| . \ _i \right\rangle\right|^2 \delta(E_f - E_i - \hbar . \ ) \tag{2.6}$$

where $i, f$ denotes the initial and final states, $\Psi$ is the electron wave function, $E$ represents the energy state of electron, and $. \ = 2\pi . \ .$ is the radian frequency of the absorbing photon.

Solving the above equation reveals that, in a symmetrical well, the electron transition of initial state H1 to final state E2 would not be possible due to interaction of odd (H1) and even (E2) orthogonal wave functions (see Fig. 2-3). One possible solution is to create an asymmetrical well such that the two states in question (H1 and E2) are not orthogonal to each other. After implementing the asymmetric design, the final device had the characteristics described in Table 2-1 [1].

| | Substance | Mole % In | Thickness (A°) | Si Doping Concentration ($cm^{-3}$) | Description |
|---|---|---|---|---|---|
| | GaAs | | 5000 | 1E+18 | cap layer |
| 25x | GaAs | | 300 | --- | Barrier |
| | InGaAs | 10 | 40 | --- | Small well |
| | InGaAs | 30 | 40 | 1E+18 | Large well |
| | GaAs | | 500 | --- | Barrier |
| | GaAs | | 5000 | 1E+18 | Buffer |
| | GaAs | | 6.35E+06 | --- | SI GaAs |

Table 2.1 Wafer specifications as provided by IQE Inc. The 25x bracket indicates the device consists of twenty-five layers of the highlighted regions (yellow). (From [1].)

The final quantum well structure is shown schematically in Fig. 2-4:

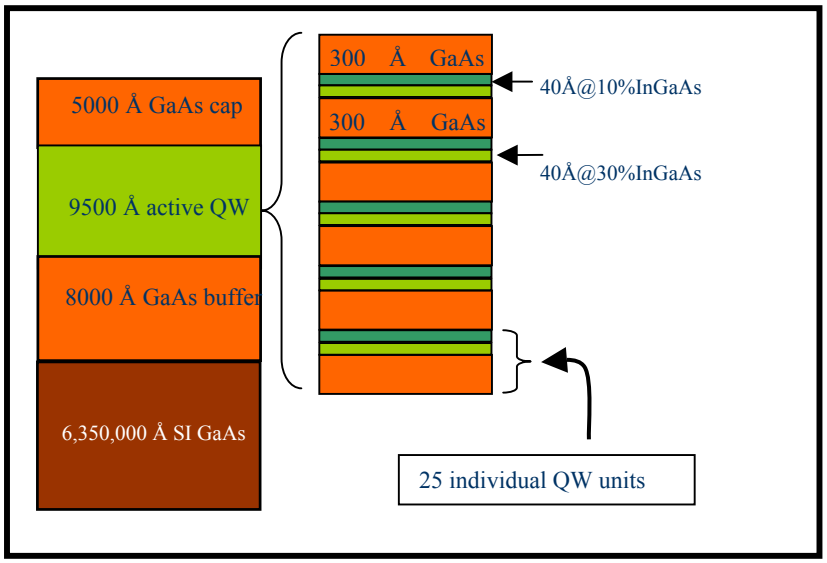


Fig. 2-4 Illustration of material composition in a two-color QWIP structure (After [1].)

Two different design patterns were created in order to evaluate device's performance in a multi-element array sensor. The first device was based on a round quantum-well area with a circular metal contact on top (Fig. 2-5a.). The second device was formed

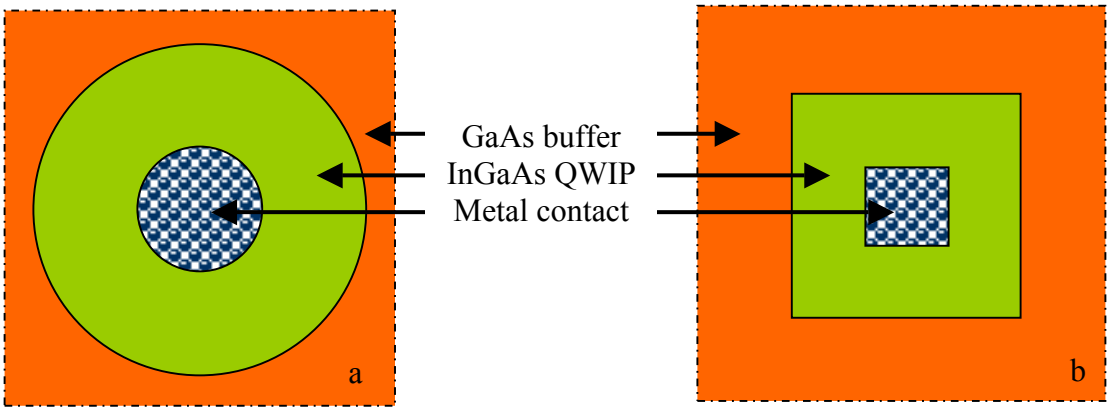


Fig. 2-5. Illustration of two-color QWIP designs used in this thesis (After [1].)

with a square active area and a square metal contact (Fig. 2-5b.). In addition, the size of the active area (the green regions in Fig. 2-5) in each design was varied from one element in the array to the next. This was done to evaluate performance as a function of size and shape of the active area. An image of the actual device with square and circular active area designs is shown in Fig. 2-6.

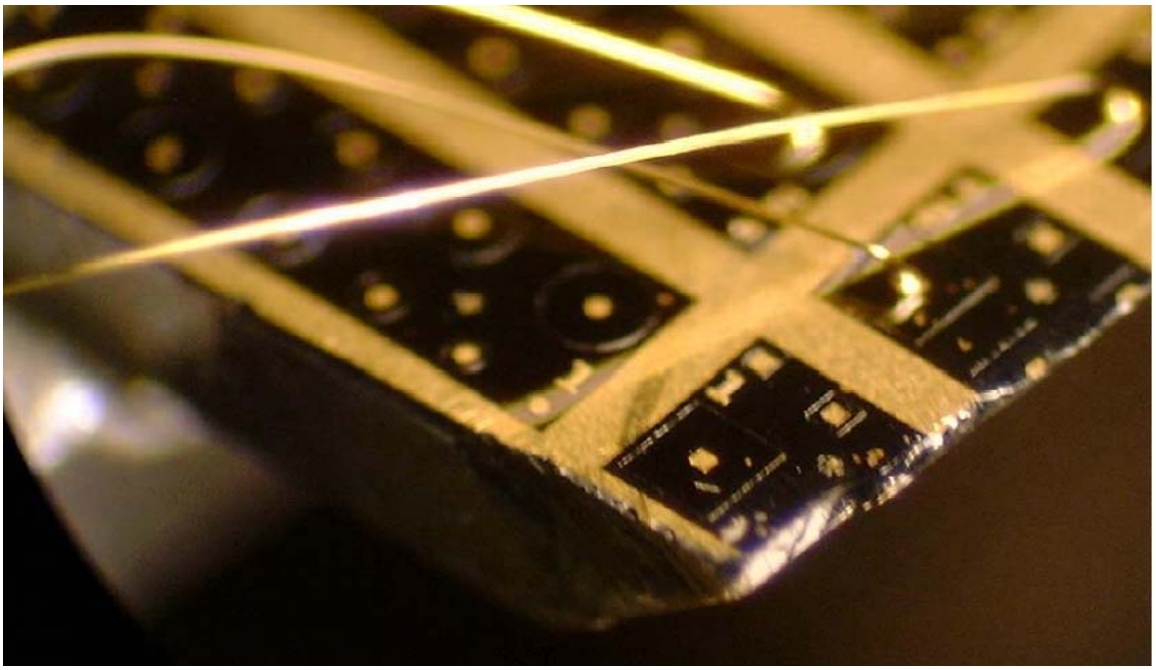

Fig. 2-6. Magnified image of two-color square and circular QWIP devices. Gold bonding wires can be seen connecting metal contact to external circuitry. (From [1].)

This chapter has described the theory behind a dual band, asymmetrical quantum well design using InGaAs/GaAs material. The physical structures described above were used in all subsequence experiments to measure material quality, transport parameters, and to determine the suitability of InGaAs/GaAs as the principle material to build a dual wavelength quantum-well IR photodetector. That is the main topic of the next two chapters.

# III. CATHODOLUMINESCENCE AND PHOTOLUMINESCENCE STUDIES OF InGaAs/GaAs QUANTUM WELL INFRARED PHOTODETECTOR (QWIP)

## A. INTRODUCTION:

This chapter describes the principles of cathodoluminescence (CL) and photoluminescence (PL) techniques and their application in characterizing material properties of InGaAs/GaAs QWIPs. The experimental systems are described and luminescence data are presented and evaluated.

Luminescence is the emission of light in response to external excitation. The source of excitation could be particle in nature as in electron/ion stimulation or it could be in the form of incident electromagnetic radiation (photons). Cathodoluminescence is a process of generating luminescence using electron beam bombardment of the specimen and subsequently analyzing the characteristics of the emitted light. Photoluminescence, on the other hand, relies exclusively on photo-excitation to stimulate light emission in the material.

In most semiconductor materials, absorption of electrons or photons with $E > E_g$ can lead to the production of electron/hole pairs. When these electron and hole pairs recombine, they can produce light with wavelengths and intensities that are related to material properties (or more appropriately the energy structure of material). Both CL and PL techniques rely on these specific properties of the emitted light to provide information about the electrical and optical properties of the material. However, there are some differences in these two techniques that need to be elucidated. The main differences between CL and PL are in the details of electron-hole pair excitation. Specifically, it is differences in generation rate and excitation volume [2] that can result in different spectra for CL and PL investigation of the same material.

From a generation rate point of view, a 20-keV electron in CL can create thousands of electron-hole pairs through multiple absorption/scattering mechanisms [2] (i.e., backscatter electrons, secondary electrons, elastically scattered electrons, etc.). In PL a single absorbed photon generates only one pair of electron-hole per interaction. In both cases, some fraction of the absorbed energy is released as heat in the form of phonons.

The other difference between the two techniques is the excitation volume. The PL excitation volume is determined by $V = A \cdot D$, where $V$ denotes the volume of excitation, $A$ is the incident area, and $D$ is the depth of light penetration. For a constant area, the excitation volume is controlled by the depth of penetration $D$, which in turn is determined by the absorption coefficient of the material, also known as Lambert's law:

$$I(x) = I_0 e^{-\alpha x} \tag{3.1}$$

where $I_0$ is the initial intensity at the surface, $\alpha$ represents the absorption coefficient ($cm^{-1}$), and $x$ is the depth of penetration (in cm). For green light incident ($. = 514\,nm$), $\alpha$ in GaAs is measured to be around $6 \cdot 10^4$ $cm^{-1}$ or 6 ∝m$^{-1}$. As a result, most of the incident photons (99%) are absorbed within the first 0.77 ∝m of the surface. It is this shallow depth of light penetration $D$ for photons with energy $E > E_g$ that limits the excitation volume in PL of semiconductor materials.

On the other hand, cathodoluminescence provides analogous information as in PL but with the additional advantage of depth penetration. By varying the energy of the electron beam, the CL process allows some control of the electron penetration depth in the material [2]. Fig. 3-1 illustrates the volume generated as a result of electron trajectories

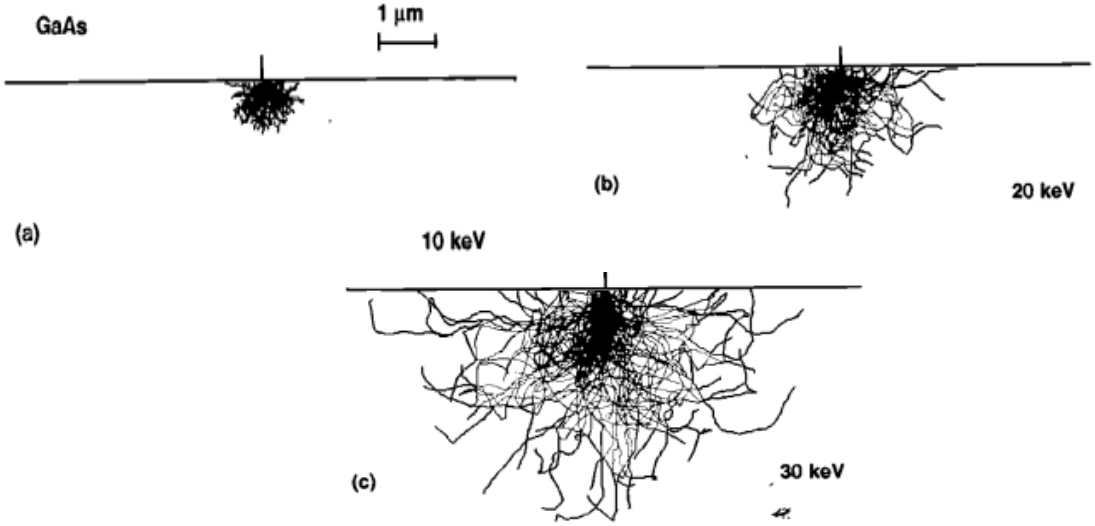


Fig. 3-1. Monte Carlo simulation of electron trajectories in GaAs as a function of kinetic energy. [2].

in bulk semiconductor material for three different values of excitation energy. Unfortunately, it is difficult to model the electron scattering path in a solid since this is a highly random process.

Using statistical methods and Monte Carlo simulations, there have been several efforts to develop an expression to describe electron penetration in a solid. The most commonly used models are those of Kanaya-Okayama and Everhart-Hoff [2]. The upper bound range of electron beam penetration can be described by Kanaya and Okayama [2]:

$$R_{e\_upper}[\mu m] = \frac{0.0276A}{. Z^{0.889}} E_b^{1.67} \tag{3.2}$$

where $R_{e\_upper}$ is the range of electron penetration in ∝m, $A$ is the atomic weight in g/mol, $.$ is density in g/cm$^3$, $Z$ is the atomic number, and $E_b$ is electron beam energy in keV. The lower bound for electron penetration is described by the Everhart-Hoff expression [2]:

$$R_{e\_lower}[\mu m] = \frac{0.0398}{.} E_b^{1.75} \tag{3.3}$$

Using average density for Ga and As, the two expressions above are plotted in Fig. 3-2 and the actual range of electron penetration in GaAs should fall somewhere between these two curves.

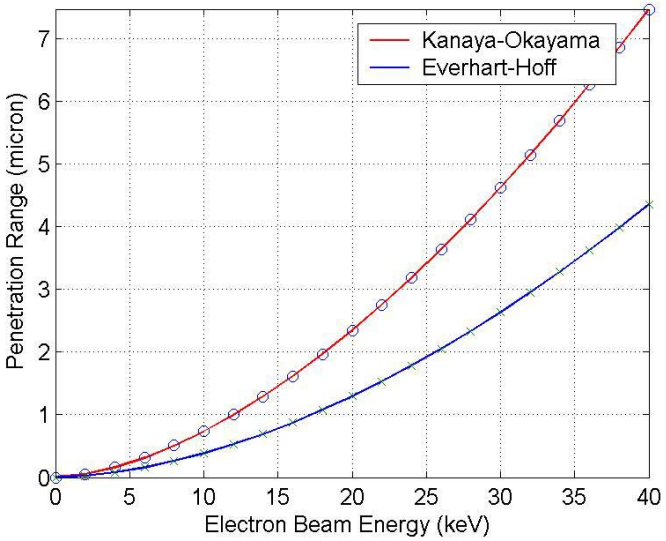


Fig. 3-2. Electron penetration in GaAs as a function of energy.

Knowledge of electron beam penetration is important because we can use it to excite the luminescence in multiple-layer materials such as QWIPs.

In this section, we described the application of CL and PL to examine luminescence from an Indium Gallium Arsenide (InGaAs) dual color QWIP device. We utilized the SEM (Scanning Electron Microscope) facility in the Physics Department at the Naval Postgraduate School (NPS) to perform cathodoluminescence analysis. The present detector setup at NPS for standard CL limits the wavelength collected from 400 nm to 900 nm. Data from CL experiments were supplemented by a photoluminescence experiment performed by the author at Lawrence Berkeley National Laboratory (LBNL). This system has the capability to collect spectral data from 800 nm to 1800 nm. The important parameters needed from CL and PL studies are the emission spectrum, intensity, and the full-width at half-max (FWHM) characteristics of the light emitted from the material. These provide information on both the electronic structure and the quality of the material.

## B. CL ANALYSIS BASICS AND PROCEDURES:

### 1. Basics of Cathodoluminescence

There are two types of interactions that take place as an electron encounters atoms in a solid, elastic scattering and inelastic scattering. For the most part, it is the inelastic scattering that gives rise to useful information such as secondary electron emission, luminescence and characteristic x-rays [2].

### 2. CL Experimental Setup and Procedures

The basic building blocks of an SEM are shown in Fig. 3-3 and short descriptions of each component are provided below.

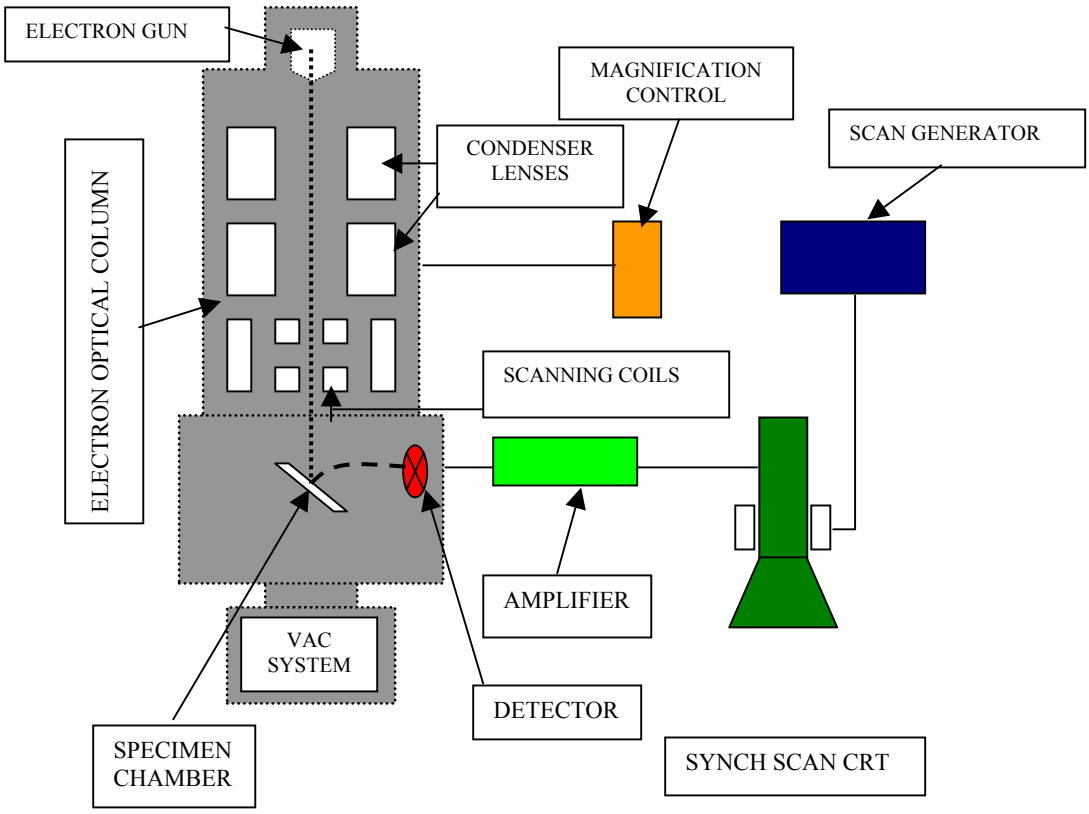


Fig. 3-3. Block diagram of a SEM (Adapted from [2].)

An electron-optical column, also called a Wehnelt cylinder, is used to confine electromagnetic radiation and serves as the housing unit for other components. This unit is maintained under vacuum of about $10^{-6}$ torr.

At the top of the cylinder is an electron gun. This gun generates a beam of electrons from thermionic emission of a tungsten filament. By applying a voltage potential anywhere from 1 – 40 kV, the kinetic energy of emitted electron can be precisely controlled.

Electromagnetic fields from a set of condensers and objective lenses are used to form and focus the thermionic electrons into a circular beam of about 50 Å in diameter [2].

When this electron beam makes impact with the specimen, secondary electrons are collected by the detector for display on the screen.

In applying cathodoluminescence techniques, there are two possible modes of operation, imaging CL and spectroscopic CL. Imaging CL uses scan locations of the elec-

tron beam in a SEM to map the luminescence intensities given off as a result of electron-material interaction. The result is a 2-D image of intensity versus spatial location data and this is the basis of the imaging CL technique discussed in Chapter IV.

In spectroscopic CL, the luminescence from electron beam bombardment at a fixed point is collected and separated into its wavelength components for analysis. In order to do this, a set of light collecting and analyzing devices are needed in addition to the normal SEM detector setup. A parabolic mirror mounted on a movable arm is inserted into the specimen chamber. This mirror has a small hole to allow the electron beam to pass through and to impact the specimen. This parabolic mirror can collect about 85% of the luminescence given off the sample. Light reflected off the mirror is directed toward a slit in the entrance of a monochromator. A diffraction grating inside the monochromator separates the incoming light into its wavelength components. The energy spectrum of the emitted light can be obtained from measuring the photon counts in each wavelength interval using a photomultiplier tube. Spectroscopic CL experimentation and data analysis are discussed in section below.

### 3. Experimental Setup

The CL analysis used in this experiment was performed using a JEOL 840A series SEM (Fig. 3-4). An Oxford Instruments monochromator with an extendable parabolic mirror arm was attached to the side of the electron optical column to perform the CL analysis. A Hamamatsu GaAs photomultiplier tube (PMT) was used in photon counting mode. Using thermoelectric cooling, this device operated at –20°C to reduce dark current.

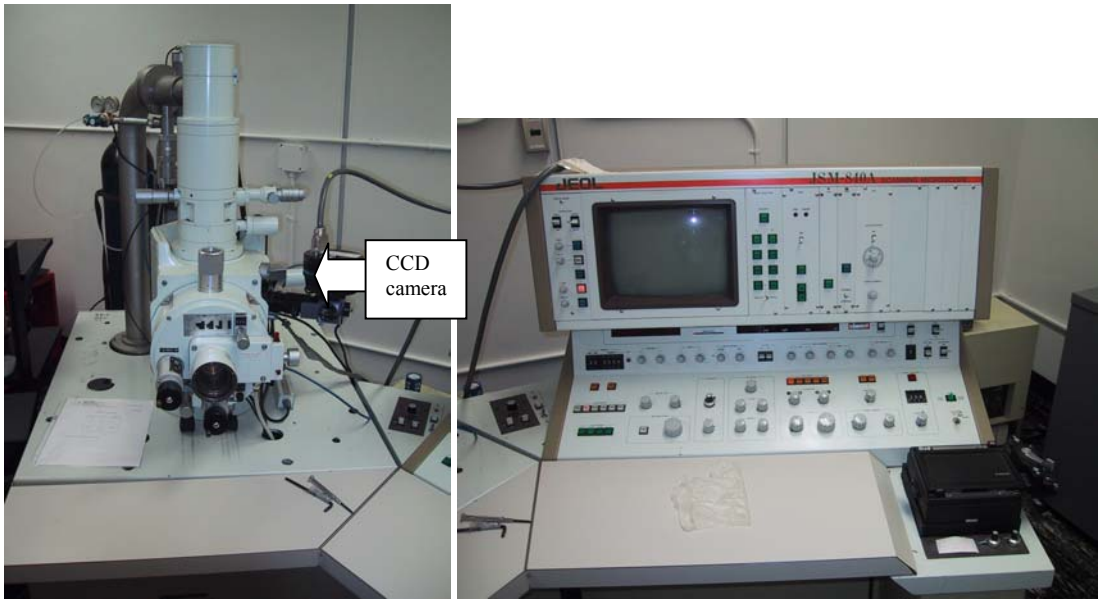


Fig. 3-4. Scanning Electron Microscope used in collecting CL data.

The following settings were applied to the CL system during spectroscopic data collection. The SEM magnification was set at 200,000X, the probe current was set to 10 nA and the accelerating voltage was 35 kV. Both the front and the back slits of the mono-chromator were set at 2.25 mm for light collection. The monochromator was programmed to sweep the spectrum from 750 nm to 900 nm with steps of 1 nm.

CL data for the substrate and the quantum-well layers were collected using two small samples of the original material. The first piece contained the InGaAs quantum-well devices sandwiched between the GaAs cap and substrate layer. This material was analyzed with electron excitation energy set to 35 kV. The same test was also repeated at 15 keV. A second piece was mounted upside down so analysis of the substrate could be performed. Results from CL analysis are displayed in Fig. 3-5.

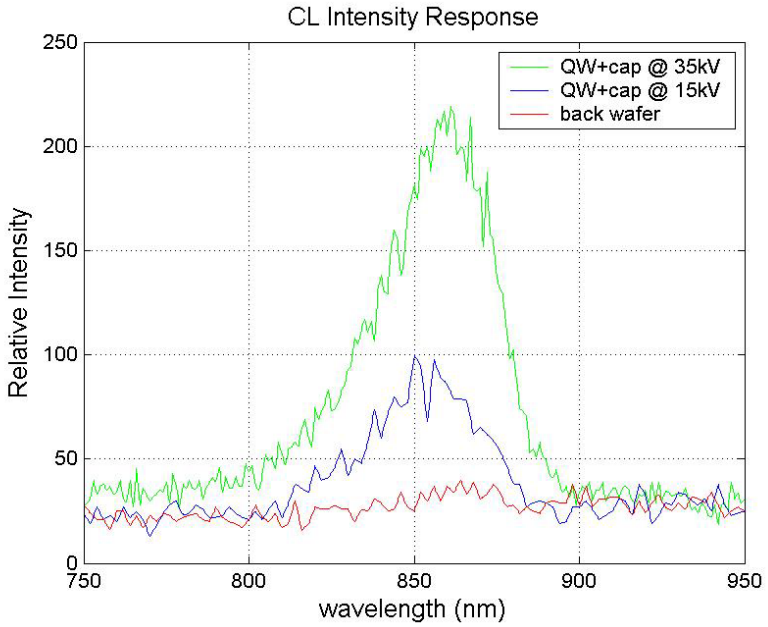


Fig. 3-5. CL spectrum of different components in InGaAs QWIPs.

The peak intensity (green curve) was recorded at 858 nm for the quantum-well and the cap layer at 35 kV electron beam excitation setting. This value corresponded to the peak emission wavelength of GaAs. The FWHM value for this device was calculated to be 44 nm at the 35 kV excitation voltage. Data taken at the 15 kV (blue curve) showed a similar trend as above, albeit at slightly lower intensity level. Data for the backside of the sample showed no measurable luminescence within the frequency scan. This was due to the fact that it was made out of semi-insulating GaAs and this material has much weaker luminescence under similar excitation condition.

Next, we collected CL data for the InGaAs quantum-well sample using increasing excitation energies. This was done to see if the spectral response of this material would change at different electron excitation energy. Spectra were measured at 15, 25, and 35 kV and the data are plotted in Fig. 3-6. This data showed an increase in luminescence intensity from the GaAs layer with increasing electron energy. At 35 kV, the relative intensity was almost twice the value at 15 kV. This is due mainly to the decreased influence of surface recombination at high electron penetration energy. The important result in this experiment was that the peak response for all three different excitation energies remained the same at 860 nm.

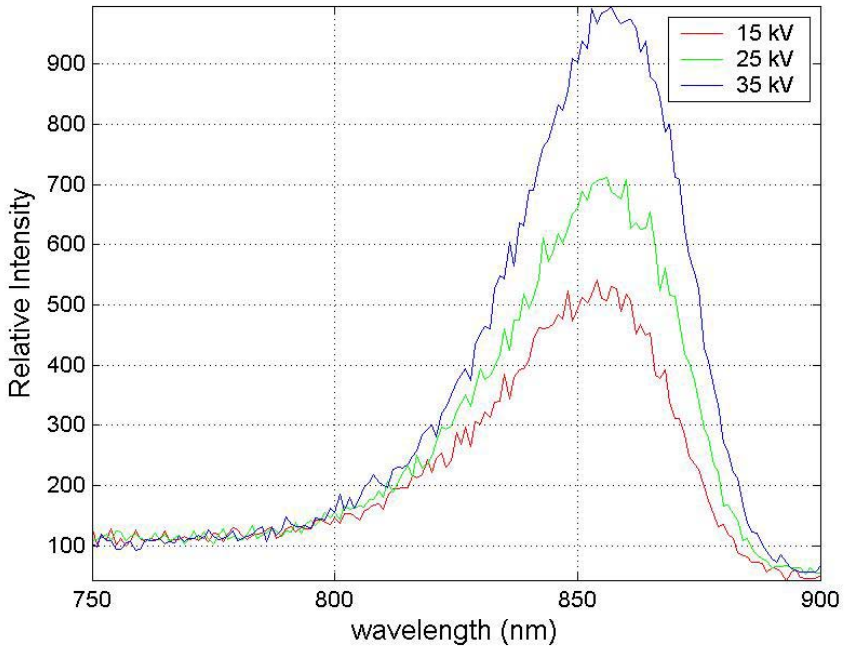


Fig. 3-6. CL data for InGaAs QWIPs at different excitation voltages

CL data were essential in determining the spectral characteristics of the semiconductor device. As will be seen in the next chapter, CL imaging is a powerful tool for analyzing material uniformity. Unfortunately, the CL spectroscopic system in our laboratory did not have the range to cover the full wavelength range of interest (e.g., the InGaAs luminescence peak at 1060 nm). For data in the range 900-1300 nm, we reverted to PL analysis and that is the topic of our next discussion.

## C. PHOTOLUMINESCENCE ANALYSIS SETUP AND PROCEDURES:

### 1. Basics of Photoluminescence

A typical photoluminescence material characterization system (shown in Fig. 3-7) consists of the following components:

1. Coherent light source (laser)
2. Beam modulator (programmable optical choppers)
3. Sample holder
4. Vacuum pump unit

5. Cryogenic system
6. Monochromator coupled to a highly sensitive detector
7. Data acquisition computer to collect detector readout

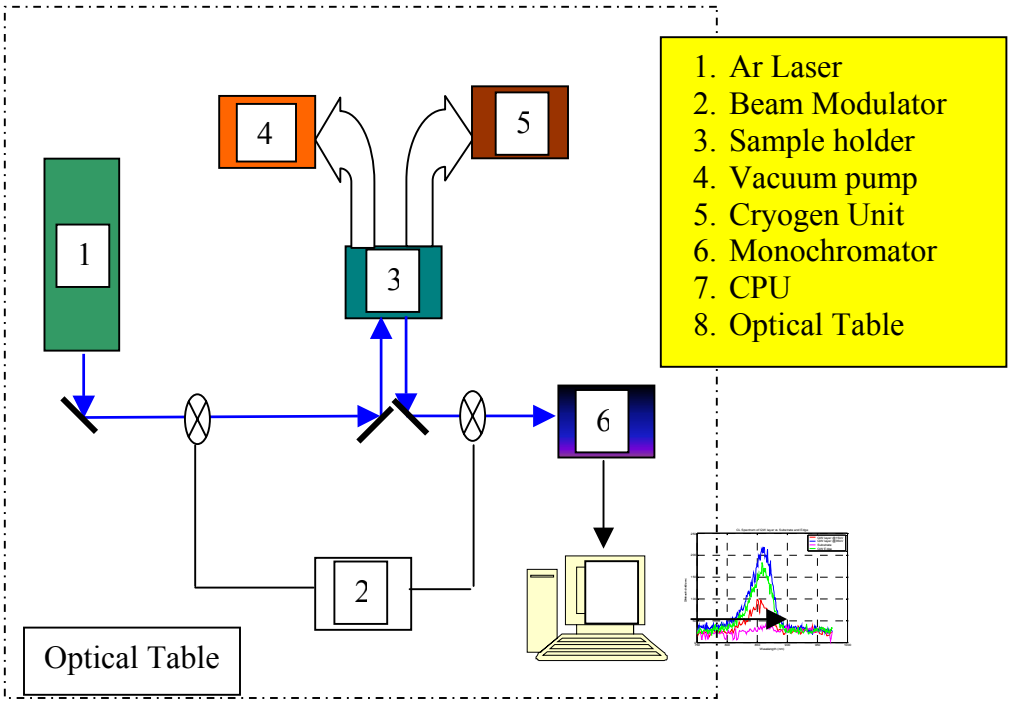


Fig. 3-7. Schematic of PL system setup

A $TEM_{00}$ gas laser is usually the source of choice for the light source (block 1) in a PL system. The output of this laser is modulated by two sets of programmable chopper wheels (block 2). The first set is located at the output of the laser while the other set is positioned just in front of the monochromator (block 6). During operation, these two sets of optical choppers have their phase set 180º apart so that the output of the laser beam would be blocked during the sample luminescence readout and vice versa. The modulated output of the laser beam is steered by mirrors to irradiate the sample through a window in the sample holder. The sample holder has an integrated vacuum system and a cryogenic unit, allowing operation to ~10K.

When photons from the laser beam are incident on the material, two types of interaction occur. If the energy of the incident photon is greater than the bandgap separation between the valence band (VB) and the conduction band (CB), absorption will take

place and one electron-hole pair is generated per incident photon. If the incoming photon is less energetic than the bandgap energy, this photon will be allowed to pass through unimpeded, i.e., the material is transparent, to first order, to this particular wavelength of radiation. Figure 3-8 illustrates this process in chronological order.

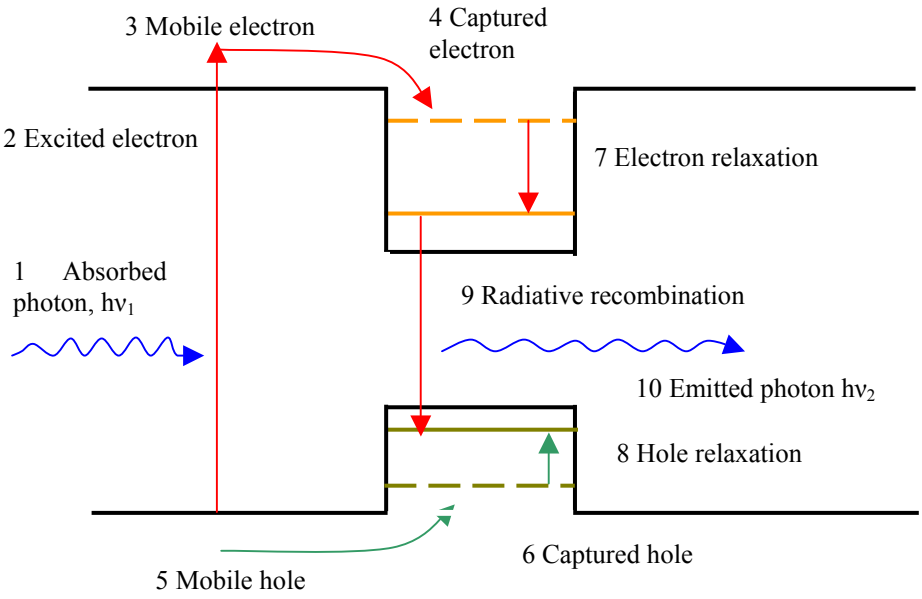


Fig. 3-8. Electron-hole generation and recombination (Adapted from [3].)

Luminescence can only be produced in the case of photon absorption. The excited electron in the CB migrates away from the generation point by diffusion and gets captured at a site in the crystal (recombination center) [2]. The electron remains in this stage until a mobile hole gets captured in the same region. Under this condition, the electron and hole will recombine to produce a photon with frequency . 2. The average time for electron and hole to recombine is the lifetime, $\tau_r$. At this point, the input photon from the laser is blocked off by the first set of chopper wheels, allowing the photon from the electron-hole recombination to emerge from the specimen. It is these photons that are allowed to pass through the second set of optical wheels and enter the monochromator (block 6). After passing through a narrow slit, these photons encounter a diffraction grating where the wavelengths are sorted by the process of interference. A sensitive germanium (Ge) photo diode is set to scan through the different wavelengths and record the intensity per wavelength interval. This output is recorded via a data acquisition card in a computer.

The important physical parameter collected from this experiment is the wavelength distribution of emitted photons. This spectrum is determined by the energy differences between the electron and hole in the recombination center. By analyzing the wavelength distribution, we can deduce the energy states in the material.

## 2. Experimental Setup:

The laser source used in this experiment was an argon ion gas laser producing 30 mW of output power at a 515-nm wavelength. The photon energy from this source is:

$$h. \ [\text{eV}] = \frac{hc}{.} = \frac{(4.135 \cdot 10^{-15})(3 \quad 10^{8})}{515 \cdot 10^{-9}} = 2.41 \text{ eV}. \tag{3.4}$$

(Notice the value for Planck's constant is in eV•s instead of J•s). The wavelength span for the monochromator was set from 750 nm to 1800 nm with increment steps of 2 nm. Within the region of interest (900 nm–1100 nm), the incremental step was reduced to 0.5 nm to obtain higher resolution of the spectral response. The detector used in data collection was a Ge pin photodiode with the spectral response curve shown in Fig. 3-9

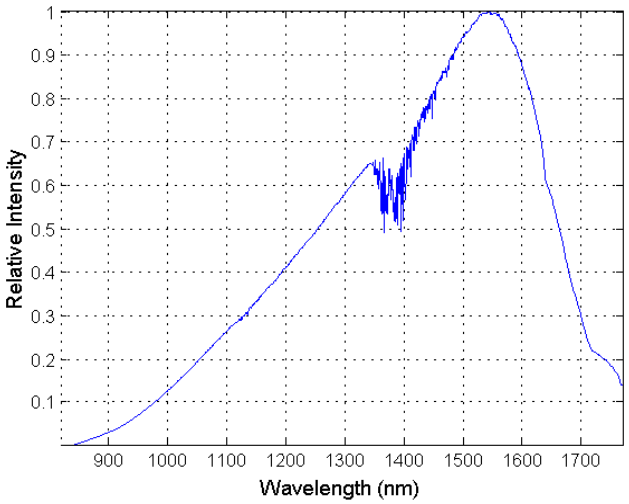


Fig. 3-9. Spectral response of Ge 850 pin detector.

The data collected is normalized by the curve above in order to obtain the true spectral response of the sample. The slit setting in the monochromator was set at 1 mm for most of the data collection except at high resolution where this slit width was reduced to 0.9 mm.

Three sets of data were collected. First was the InGaAs QWIP intensity versus wavelength at ambient temperature (295K). This data spanned from 800–1800 nm in steps of 2 nm. This was done so that result could be compared against CL data taken at room temperature. The second set was also of InGaAs at 12K but the spectrum was recorded in high resolution (0.5 nm from 900–1100 nm). Finally, a spectrum was obtained for a sample of AlGaAs to be used as a comparison with the InGaAs sample. Data for this sample were also taken at 12K.

### 3. Data Analysis:

Since the increment interval for collected data was not uniform (0.5 nm for some and 2 nm for other), a Matlab script was created to linearly interpolate data points for all data sets to allow for common normalization. These results are plotted in Fig. 3-10, showing that the device response peaked at 1019 nm for the room temperature data versus 956 nm and 972 nm for the same device at 12K. The shift of peak response toward

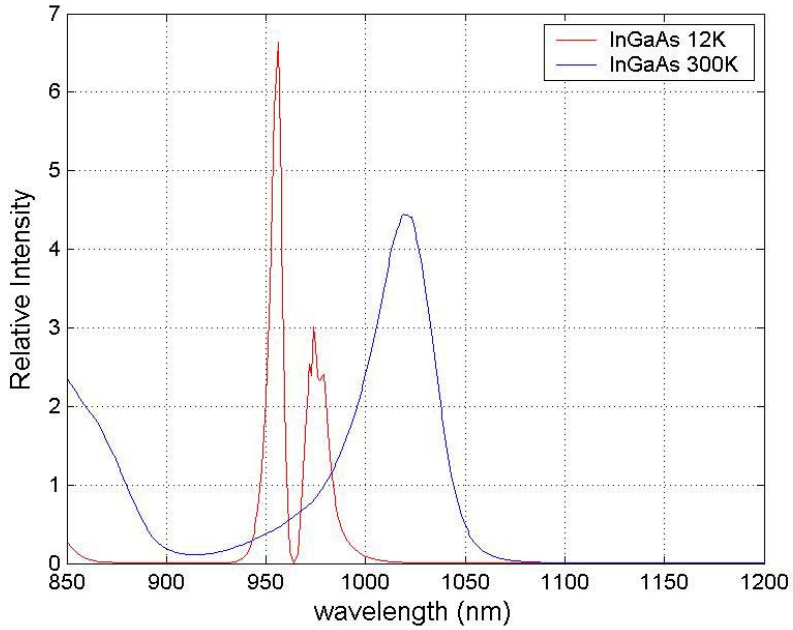


Fig.3-10. PL spectral data for InGaAs QWIP at different temperature

shorter wavelength at lower temperature was expected because the bandgap of InGaAs increases with decreasing temperature [2]. The single room temperature peak at 1020 nm becomes into two peaks at 956 and 972 nm, respectively, for 12K operation. This corre-

sponds to an energy difference of 21.3 meV. According to the energy-momentum diagram (*E-k*) for GaAs, there are two types of holes in the valence band, a heavy hole and a light hole (see Fig. 3-11). Experimental data seems to show that the first peak (956 nm) is the result when an electron in the CB recombines with a heavy hole, whereas the second peak (972 nm) is due to electron recombination with a light hole. The effective mass of light hole and heavy hole is illustrated in the energy-momentum (*E-k*) diagram below. At momentum other than zero, the energy for these two particles will be different.

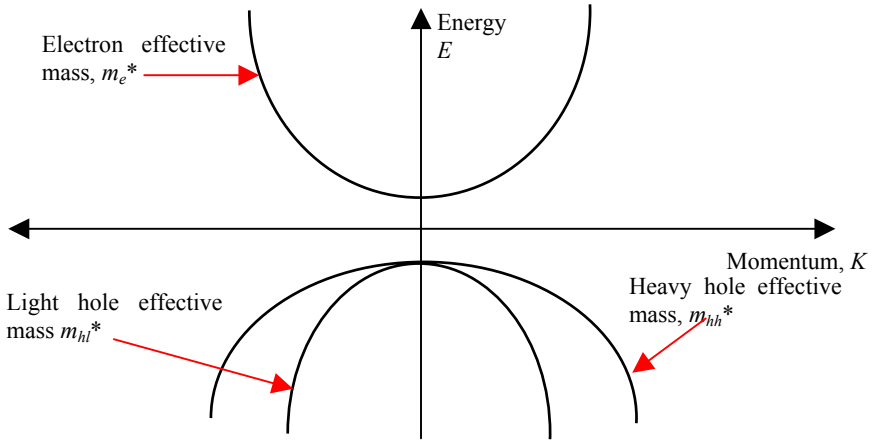


Fig. 3-11. An energy band diagram of GaAs structure showing differences in light and heavy hole.

The same set of spectral data is plotted using a logarithmic scale in the vertical direction to illustrate the relative strength of each peak in the region of interest (Fig. 3-12).

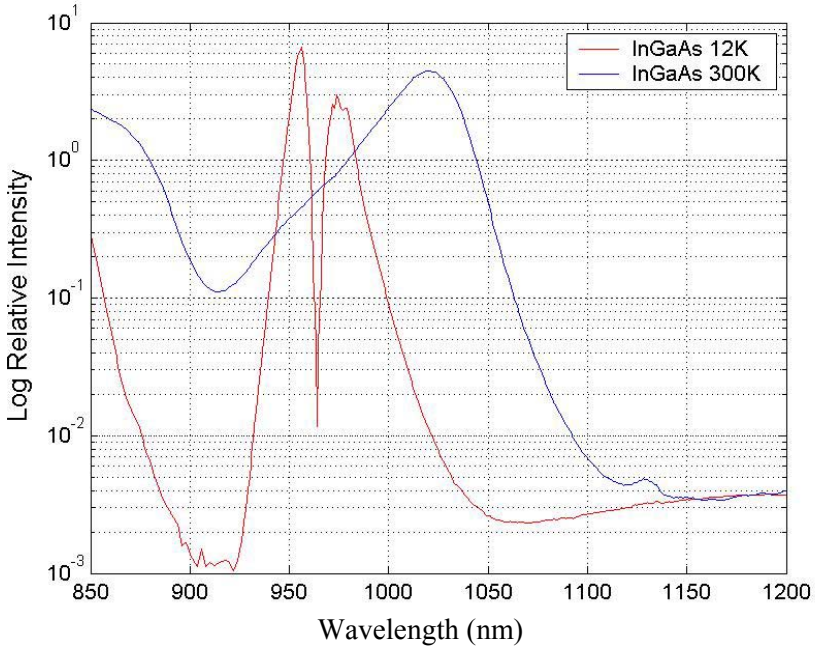


Fig. 3-12. PL spectral response in semi-log scale for InGaAs at different temperature.

The discussion above illustrates standard CL and PL experimental techniques as applied to material characterization of InGaAs/GaAs quantum-well materials. Spectral data collected were used as a basis to select bandpass filters for the imaging CL work that is discussed in the next chapter.

THIS PAGE INTENTIONALLY LEFT BLANK

# IV. CL IMAGING OF InGaAs/GaAs QWIP

## A. BASIC THEORY

The discussion in this chapter concentrates on the application of CL imaging techniques to study the material properties of InGaAs/GaAs QWIPs. Both conventional CL imaging and a new technique called direct transport imaging have been used to provide new information on the spatial variation of material properties.

As discussed in the previous chapter, conventional CL imaging uses luminescence from the interactions of an electron beam with a material sample to create an intensity image of the light emission from the material. This task is accomplished in conventional CL imaging by mapping the detector output to a location in the computer's memory. The stored location in memory is equivalent to the electron beam's position in a raster scan pattern (Fig. 4-1).

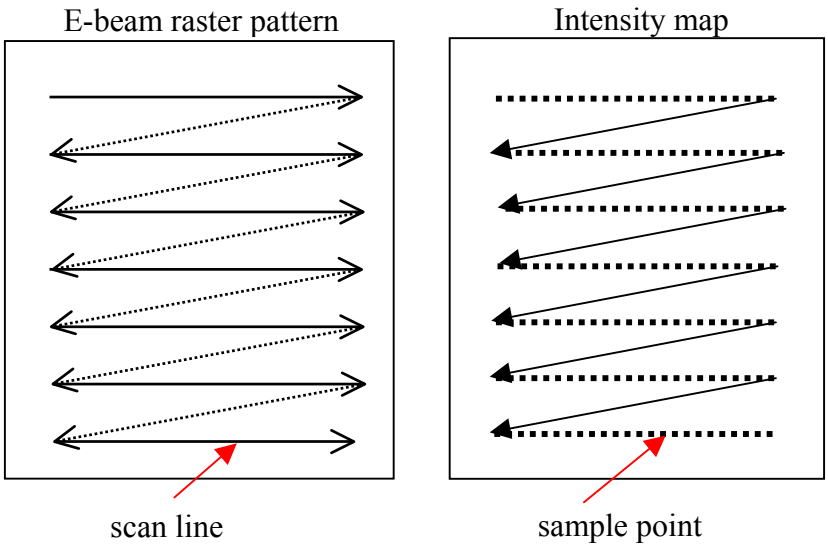


Fig. 4-1. CL imaging maps intensity of e-beam location to image.

This intensity mapping can be accomplished either panchromatically or monochromatically. In panchromatic mode, an intensity value is obtained for all photons detected by the detector independent of their wavelengths. Monochromatic mode, on the other hand, uses a diffraction grating to select a particular wavelength span. Only photons

in this wavelength range are allowed to reach the detector. The intensity value collected is then mapped to an image location for this particular wavelength only. In general, CL images in panchromatic mode have higher intensity and better contrast than those collected in monochromatic mode because of higher signal strength.

Recent work in the field of SEM imaging for semiconductor materials has resulted in a new experimental technique called direct transport imaging CL [3]. Pioneered by Professor Nancy Haegel at NPS, this method combines the resolving power of an optical microscope and the sensitivity of a CCD camera to capture the luminescence of a sample under electron beam stimulation. The advantage this method offers over the conventional imaging CL is that the spatial information of the charge recombination is preserved. Direct observation of drift and diffusion of carriers has been demonstrated with this technique in planar semiconductor structure [3]. This is illustrated in Fig. 4-2, where the drift behavior of free charges is imaged as a function of increasing applied electric field. Free holes are created at a point (see arrow) and the CCD camera captures their motion and subsequent recombination as the charges drift across the material.

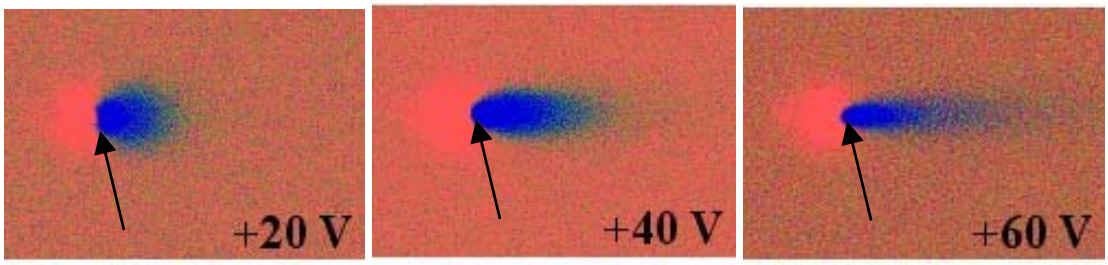


Fig. 4-2: CCD Image of spatial recombination for 20, 40 and 60 V applied between the contacts, which are ~ 1.0 mm apart. Image size is 200 (w) x 153 (h) ∝m. Dark blue indicates high intensity, red is low. A zero bias background image has been subtracted to enhance visualization of the drift behavior. (Reprinted with permission from N.M. Haegel et al., Applied. Physics Letters. **84**, 1329 (2004) [3].)

The majority of the work performed in this thesis was done using the direct transport imaging CL method as described above. Some conventional CL imaging data were obtained for comparison purposes. Experimental procedures and results are expanded in the following sections. Conventional imaging CL is described first, followed by the direct transport imaging CL.

## B. EXPERIMENTAL PROCEDURES AND DATA ANALYSIS

### 1. Conventional Imaging CL

The conventional CL imaging technique uses the same hardware system as described in the spectroscopic CL section of Chapter III (Fig. 3-3). Instead of dispersing the luminescence as a function of energy as in the spectroscopic CL case, this system collects and counts the number of photons emitted from the sample as a function of position on the sample. The photon count is assigned a relative intensity value and this quantity is mapped to the point of generation (Fig. 4-1). The output image is formed by sampling the horizontal scan line with 256 data points and stacking 192 of these lines in a vertical fashion (256 columns x 192 rows = 49,152 pixels). A set of conventional panchromatic CL images of the InGaAs/GaAs active region is displayed in Fig. 4-3.

| Accel Volt. | 5 keV | 15 keV | 25 keV |
|---|---|---|---|
| **SEM secondary electrons image** | 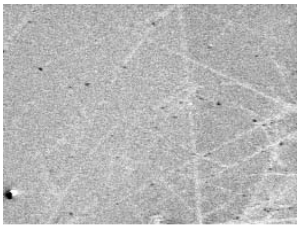 | 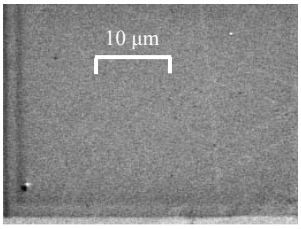 | 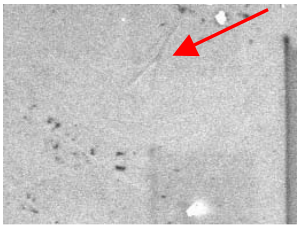 |
| **CL intensity mapped image** | 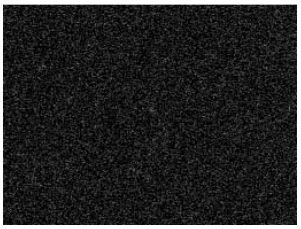 | 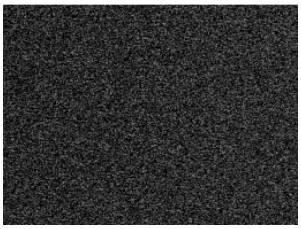 | 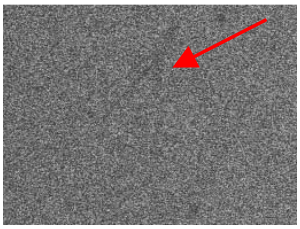 |

Fig. 4-3. Standard CL images of InGaAs/GaAs active region at different excitation voltages. SEM settings: probe current $I_p$ = 3 nA, magnification Mag = 1000X.

Pictures on the top row of Fig. 4-3 showed the digitized SEM console images in a normal scan. A scale factor of 10 μm had been included to show the size of the features displayed. The first two images on this row were taken from the same area in the InGaAs/GaAs region and the third figure was of an adjacent area. SEM console data showed some scratches on the surfaces of the first images, which became less pronounce in the second image. The reason for this trend was that, as we increased the kinetic energy of the beam, electrons penetrated deeper into the material. Hence, these surface fea-

tures became less obvious in the second SEM image. In the third SEM image, there was an inverted "Y-shaped" feature on the upper half of this image (red arrow).

The second row of Fig. 4-3 shows the conventional imaging CL data counterpart of images in the top row. Prominent surface marks of SEM images 1 and 2 could not be seen on their corresponding CL images. This was due to the fact that photons collected in conventional imaging CL mode were generated beneath the surface material. Top surface features such as light scratch marks would not necessarily affect the intensity of photons emanated from below the surface. The deep, inverted "Y" shape in the third SEM image, however, did show up in the conventional CL analogy (red arrow). This demonstrated the sensitivity range of conventional CL in detecting internal radiative structure of the material. Details near the surface would not necessary be represented in conventional CL. Features that did show up in conventional imaging CL were usually associated with internal radiative structure of the material.

### 2. Direct Transport Imaging CL

Direct transport imaging, on the other hand, focuses on the preservation of spatial information in the sample's luminescence emission [3]. The electron beam in the SEM is used, as in CL, to generate free carriers in the material. When these carriers (electrons or holes) recombine, the resulting luminescence is captured and analyzed by an external, highly sensitive silicon charge couple device (CCD) camera (Fig. 4-4). The actual system consists of a mirror with a hole for the electron beam in a SEM to pass through. This mirror has the similar construction to the one described for the CL system of Chapter III. The mirror assembly is inserted into the SEM specimen chamber using an extendable arm. An optical microscope at the end of this apparatus is used to magnify and focus the luminescence from the sample onto the CCD detector. The magnification of this optical microscope is fixed so that the resolution at the camera is 0.4 μm/pixel. To minimize the effect of noise, the CCD camera is thermoelectrically cooled to –15°C.

Depending on the operating mode of a SEM, data can be collected in scan or spot mode. In scan mode, the electron beam is swept across the sample in a raster scan pattern (Fig. 4-1). The luminescence imaging data are recorded by the camera according to the programmed exposure time. This is similar to the conventional imaging CL technique.

The difference is that the camera exposure time could be much longer than a single frame of the conventional imaging CL raster scan frame time.

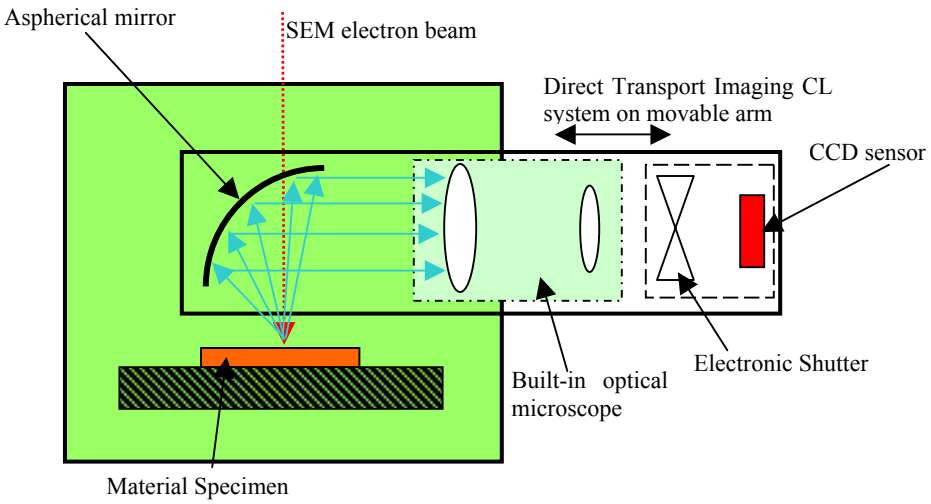


Fig. 4-4. Direct transport imaging system diagram.

Data could also be obtained in spot mode. This is the case where the electron beam of the SEM is held in a fixed position. The point of generation can be precisely determined; hence the local charge diffusion behavior can be studied. An external bias can also be applied to study mobility and drift length of the minority carriers. It is this ability to separate the charge generation from the luminescence imaging that makes the direct transport-imaging tool unique.

Using the procedures outlined above, direct transport-imaging data for InGaAs/GaAs quantum-well material were obtained with the SEM operating in both scan and spot mode. Since the information used in analyzing scanned data differed significantly from those of spot data, results for these two modes are presented separately. With the majority of the data collected in scan mode, it is presented first. Initial results on spot mode data are discussed in the following sections.

***a. Direct Transport Imaging Data with SEM in Scan Mode:***

The as-grown InGaAs/GaAs quantum-well material was used to obtain the images shown in Fig. 4-5a,b. This uniform, planar, multiple-layer material was described in Chapter II (Fig 2-4). Fig. 4-5a shows the SEM console display under the following ex-

perimental settings: probe current $I_p$ = 10 nA, e-beam accelerating voltage, $V_{accel}$ = 25 kV, and SEM magnification, Mag = 1000X. This image shows the surface topography of the sample. Notice there were no discernible structural variations displayed. Figure 4-5b presents the direct transport imaging data counterpart of Fig. 4-5a. The CCD camera's controls were set to the following values: exposure time, $T_{exp}$ = 4 seconds, temperature $T_{temp}$ = –15°C, and image size $I_{size}$ = 512 x 512 pixels. The total area of the sample imaged by the CCD camera was considerably larger than the SEM scan area under these experimental conditions. As a result, the SEM image was could be seen as the bright and rotated rectangular patch in Fig. 4-5b. Since the CCD image was acquired over several hundreds of scan cycles in the SEM's time ($T_{exp}$ = 4 seconds), the bottom edge of this image was considerably brighter than the rest. This was due to the fact that in a raster scan pattern, the electron beam was positioned longer over that particular portion of the scan. This particular feature was seen in all of direct transport imaging CL scan data.

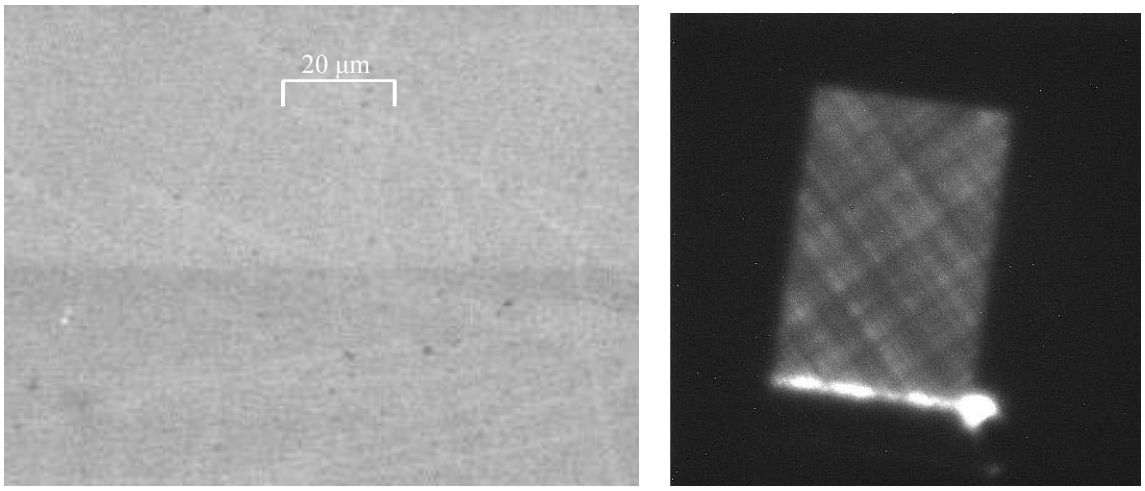


a) b)

Fig. 4-5. SEM console image and the corresponding CCD image

The most interesting features of the image acquired with CCD camera were the set of perpendicular lines as seen on the surface of the sample. These indicate a variation in luminescence efficiency over this region of material. A literature search revealed that these distinctive line patterns have been seen in other conventional CL studies [13-14]. These patterns are a result of dislocations due to lattice mismatch in the growth of InGaAs on GaAs using MBE.

$In_xGa_{1-x}As$ has a different crystal lattice value than GaAs, and during epitaxy growth, these materials (40 Å of $In_{0.1}Ga_{0.9}As$ layer plus 40 Å of $In_{0.3}Ga_{0.7}As$ layer and 300 Å GaAs layer) are relaxed via dislocation formation (Fig. 4-6). This type of line defect is known as an edge dislocation and it acts as the local non-radiative recombination center and this is reflected in the CL intensity.

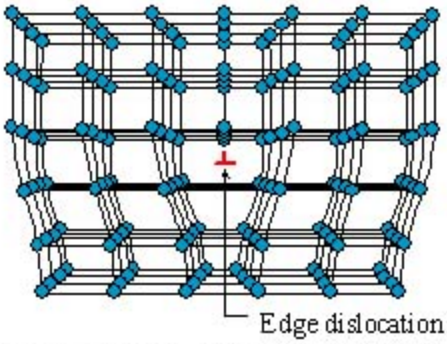


(a) Dislocation is a line defect. The dislocation shown runs into the paper.

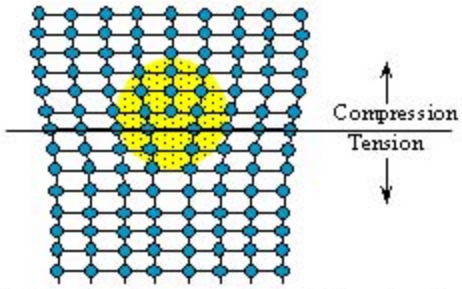


(b) Around the dislocation there is a strain field as the atomic bonds have been compressed above and stretched below the dislocation line

Fig. 4-6. Illustration of edge dislocation line formation. (From [11].)

Experiments were designed to examine the relationship between these dislocation patterns and the various experimental conditions: SEM probe current $I_p$, e-beam accelerating voltages $V_{accel}$, CCD image exposure time, and CCD temperature. Results indicated that the pattern was a strong function of the e-beam accelerating voltage and probe current, as seen in Fig. 4-7, and was very much less dependent on the CCD camera settings (exposure time, temperature). The minimum values to observe this pattern were with $V_{accel}$ set to 3 keV and probe current placed at 100 nA. The pattern became more clearly defined at higher beam energy settings of 18 keV and above (25–35 keV).

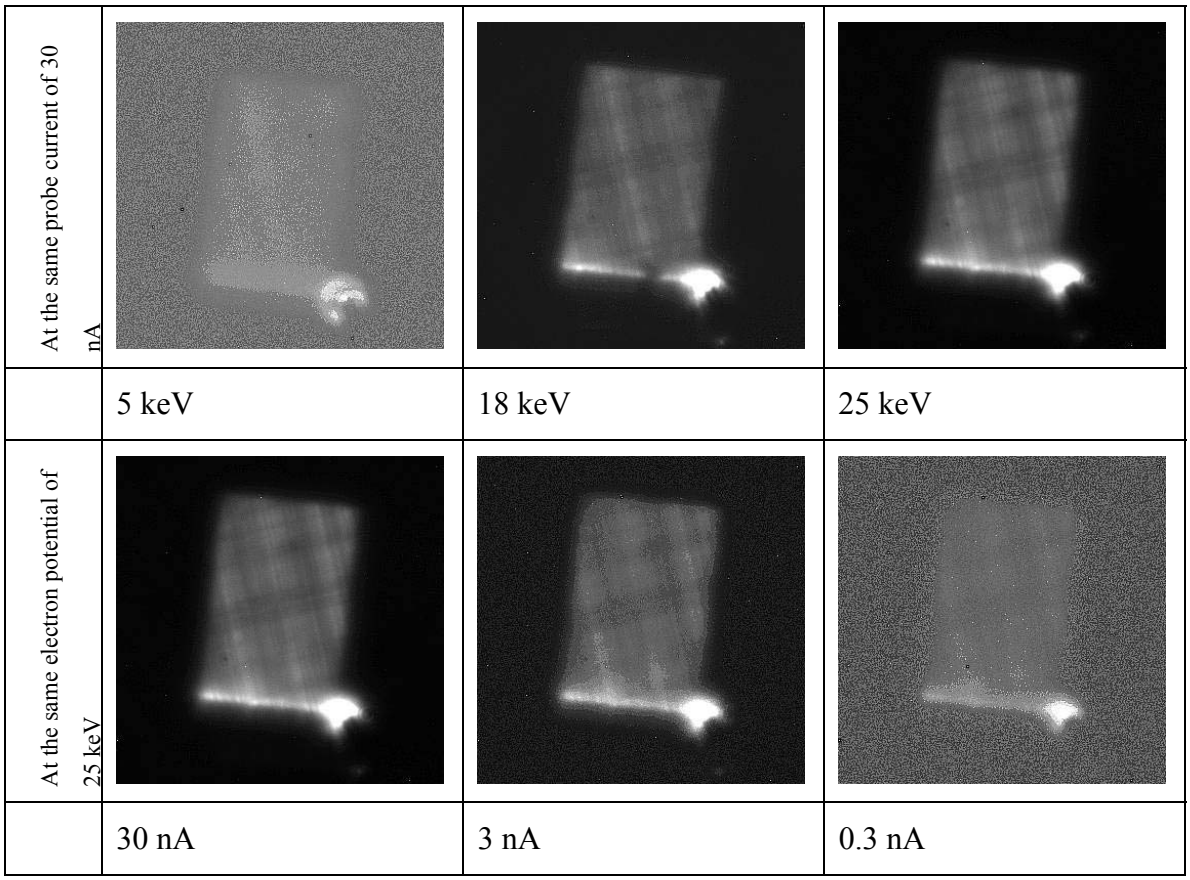


Fig. 4-7. Images of InGaAs/GaAs quantum-well material under different experimental conditions (SEM parameters).

### *b. Isolation of the Dislocation Layers*

A key question raised by the observation of the dislocation network was whether the dislocations existed only in the InGaAs or had propagated as well into the upper GaAs cap layer. Since the CCD images were taken in panchromatic mode, it would be necessary to perform monochromatic imaging to separate the InGaAs luminescence from the GaAs emission. If these dislocation patterns were the result of dislocations in the InGaAs layer only, then the emission wavelength would have the characteristic spectral peak at 1020 nm at 300K for InGaAs as measured by the PL system in Chapter III. By similar reasoning, if the dislocation patterns continued into the cap region, they would effect the characteristic emission of GaAs, which was measured by the CL system to be around 870 nm.

The spectral response of the silicon detector in the CCD camera extended from the visible region (0.4 μm) up to the NIR (about 1.1 μm). Figure 4-8 displays a set of absorption data for common semiconductor materials, including Si, Ge, and InGaAs. The resulting image from the CCD camera would encompass all wavelengths within this band. This would include both the GaAs emission as well as the InGaAs emission. To construct an experiment where we could identify the dislocation patterns with a particular layer, a set of bandpass filters was needed. Unfortunately, it was difficult to find a set of bandpass filters with the exact center wavelengths (870 nm and 1020 nm) and bandwidth of desired specifications. A solution was found instead with a set of short and long-wave pass filters that had a very steep transition region (Fig. 4-9a,b). These filters relied on interference effects rather than absorption to isolate the spectral bands.

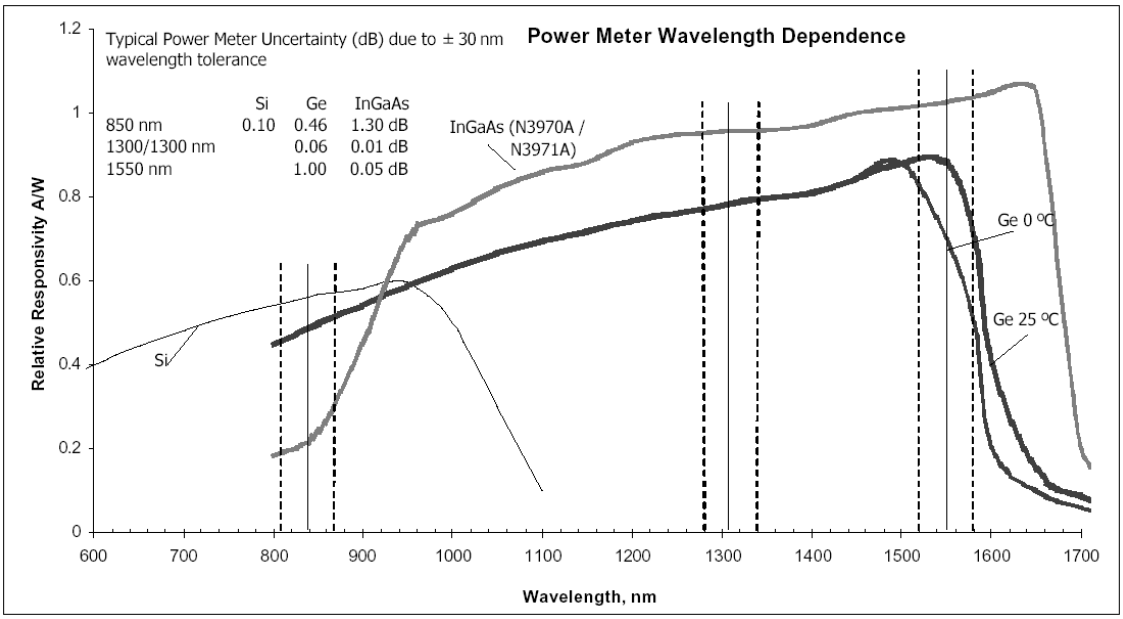


Fig. 4-8 Optical absorption in semiconductor materials (From [16].)

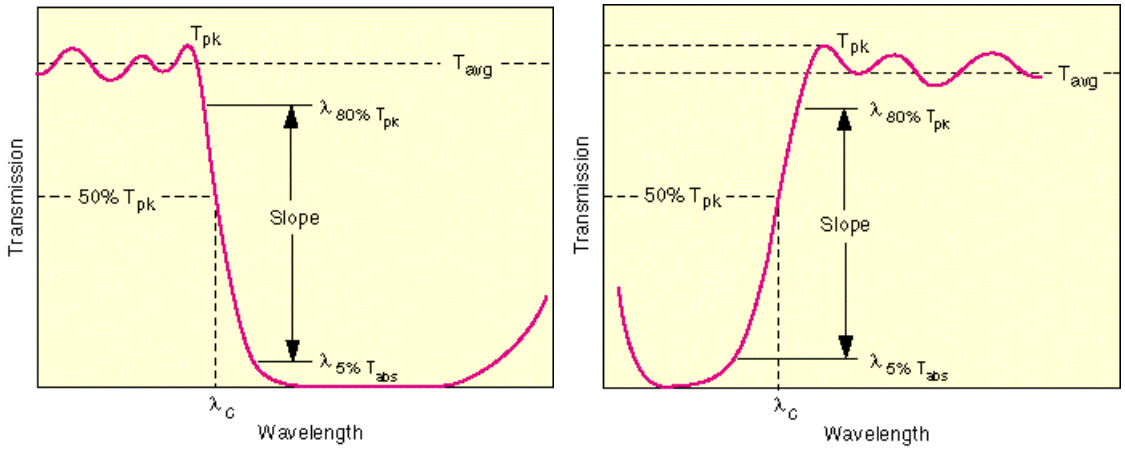


Fig. 4-9 Spectral response of the short-wave pass and long-wave pass filters (From [17].)

An experiment was designed using a piece of InGaAs/GaAs wafer with the fabricated quantum-well devices. This was done so that luminescence data from both the buffer region and the active area of the device (cap and InGaAs layers) could be viewed simultaneously. Imaging data were taken for both the round and square devices. A short-wave pass filter with blocking characteristics in the InGaAs emission range (998-1188 nm) was inserted into the optical path and in front of the CCD camera. The intention was to block any light with InGaAs characteristic emission (1020 nm). The experiment was repeated using a long-wave pass filter with blocking range in the GaAs emission (760-898 nm). Again, the objective was to remove luminescence from this layer. Results are shown in Fig. 4-10. Clearly, the dislocation pattern seen in the top row did not appear in the GaAs cap layer of the second row images. The last row of this table shows imaging data taken with the long-wave pass filter. In this case, both the round and square device clearly showed the dislocation pattern contained only in the layers with the lattice mismatched InGaAs.

| Experimental Parameters | Square device imaging data | Round device imaging data |
|---|---|---|
| No filter used | 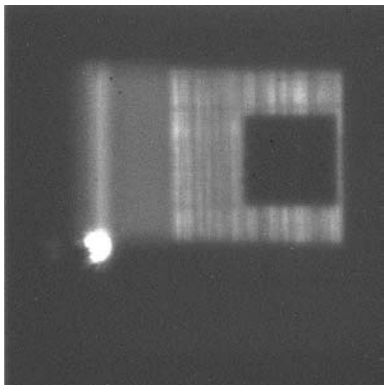 | 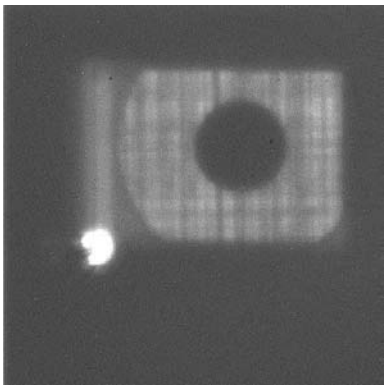 |
| Short-wave pass filter<br>Cut-off wavelength ($\lambda_c$ = 950 nm)<br>Transmission range: 400-898 nm<br>Blocking range: 998-1188 nm<br>Index of refraction ne = 1.82<br>Cat. # : 10SWF-950 | 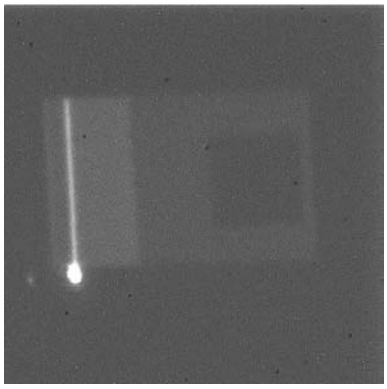 | 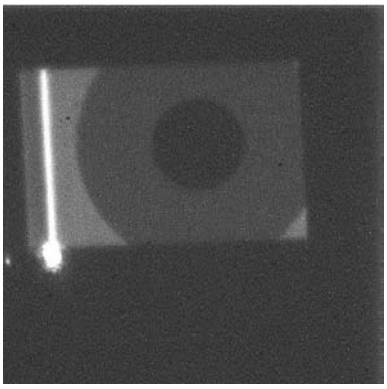 |
| Long-wave pass filter<br>Cut-on wavelength (c = 950 nm)<br>Transmission range: 1045-2200 nm)<br>Blocking range: 760-898 nm<br>Index of refraction ne = 1.55<br>Cat. #: 10LWF-950 | 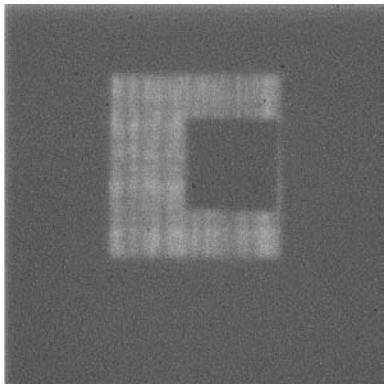 | 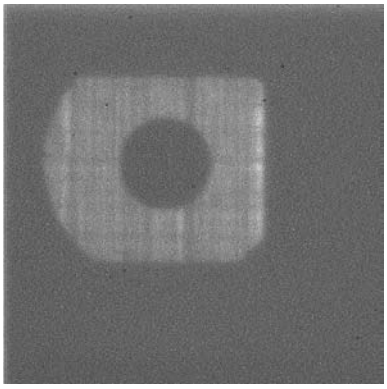 |

Fig. 4-10. Comparison of images using Si CCD camera and with short and long-wave pass filter.

### *c. Dislocation Density Measurements*

The next research goal was to estimate the number of dislocations lines per unit cm ( $\delta_x, \delta_y$ ) in the InGaAs layer. The x-direction and y-direction were defined as being parallel and perpendicular to the direction of an arbitrary dark stripe in the direct

transport image (the orange diagonal line in upper top left of Fig. 4-11). Utilizing the fact that the combination of optical microscope and CCD camera had a fixed resolution of 0.4 μm per pixel, the measured distance, in μm, is obtained by multiplying the number of pixels with this constant: $\text{distance}[\propto m] = \#\text{ of pixels} \cdot\ 0.4\ \mu\text{m/pixels}$.

The number of dislocation lines was obtained by counting the number of dark bands contained in this distance. Figure 4-11 illustrates the procedure used in determining the distance and number of dark bands in a particular direction. An intensity line pro-

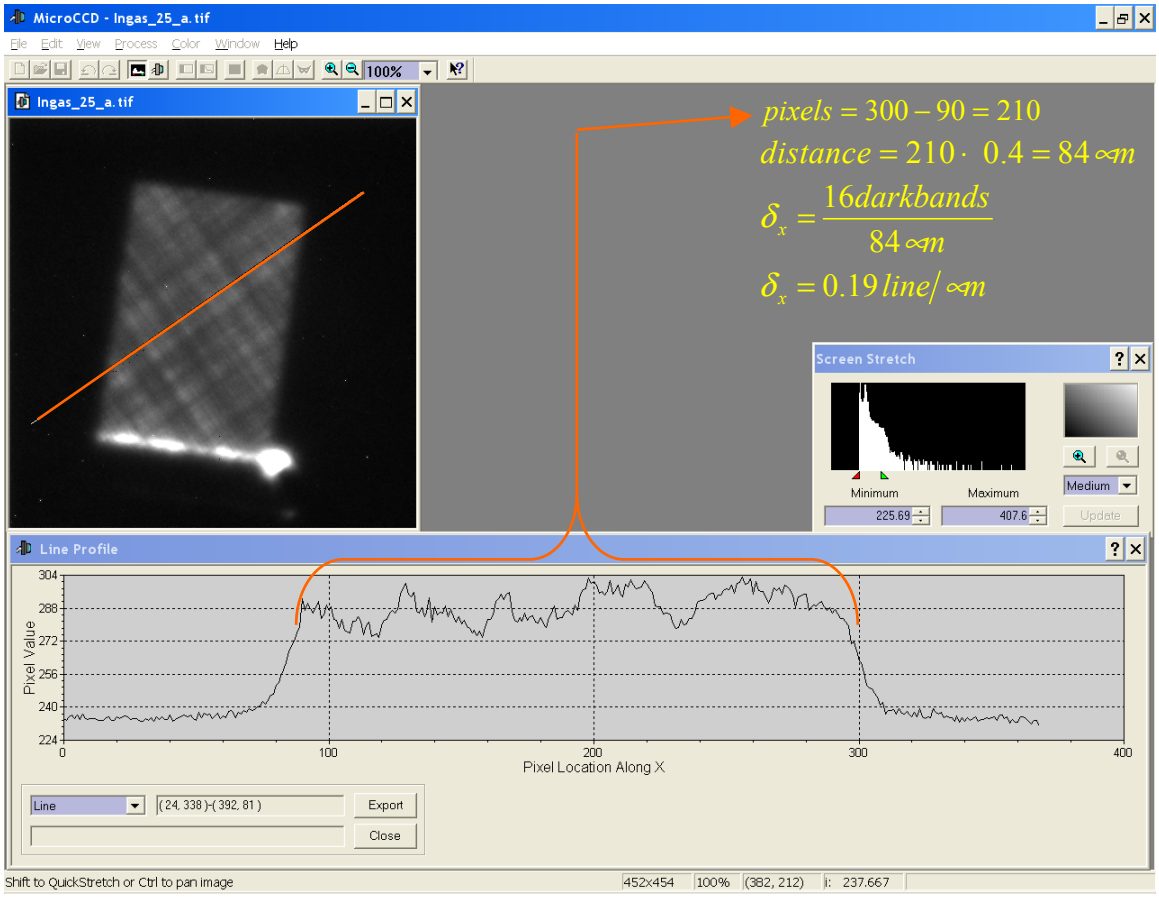


Fig. 4-11. Line intensity profile example of determining $\delta_x$

file was drawn parallel to a diagonal dark band. The number of pixels in the bright region was determined from the edges of the raised intensity level of the graph (210 pixels). The number of dislocation lines was found by counting the perpendicular dark bands in this region. Using this method, an average lines dislocation density per unit length was de-

termined to be: $\delta_x = 0.19\,\text{lines}/\mu\text{m} = 1900\,\text{lines}/\text{cm}$ for the *x* direction and by similar argument, $\delta_y = 0.14\,\text{lines}/\mu\text{m} = 1400\,\text{lines}/\text{cm}$ for the *y* direction. Other studies [7] had indicated an upper limit of about $2 \cdot 10^4\,\text{lines/cm}$ and our experimentally obtained values were well within this range. Notice that these quantitative values were determined by a combination of carrier diffusion length and the resolution of the microscope.

***d. Dislocation Lines Intensity Variations.***

Following the determination of the dislocation density, another important question was the amount of fluctuation in intensity between a dark and a bright band as seen in these direct transport CCD images. We needed to compare this value against the average intensity of the electron beam scan area to qualitatively describe the results. Using a similar approach as outlined in previous section, an average fluctuation level was determined by measuring the intensity values of a peak and a trough via an intensity line profile function as seen in Fig. 4-12. This value turned out to be about 12 intensity units for several of the images. An alternative method for measuring this quantity was to use a statistical tool to obtain the standard deviation in the scan region. We obtained a standard deviation of about 7.7 intensity units in going from a bright to dark band in the scan region. The average background intensity was calculated to be about 233. The average scan region had an intensity of about 282. The percentage of fluctuation was calculated using both the average value and the standard deviation value.

$$\text{ave. fluct} = 12, \quad \text{std. dev} = 7.7, \text{ ave. b/g} = 233, \text{ ave. scan area} = 282,$$
$$\Delta\text{signal-to-noise level} = \text{ave. scan area} - \text{ave. b/g} = 282 - 233 = 49$$
$$\%\text{change using ave. fluct} = \frac{12}{49} = 24\% \text{ , } \%\text{change using std. dev.} = \frac{7.7}{49} = 16\%$$

Fig. 4-12a displays the CCD camera image of the dislocation network. Superimposed on this image is the intensity profile line function (orange line) indicating the direction and location of the intensity map being displayed in Fig. 4-12b.

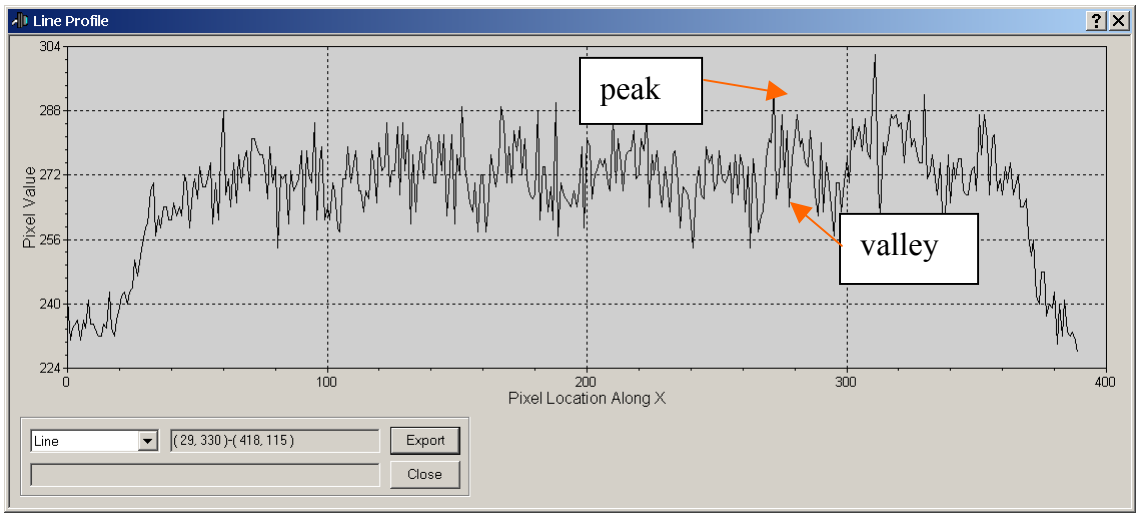


Fig. 4-12. The intensity fluctuation was determined by taking the difference between the peak value and the adjacent valley.

We applied the same analysis to several images and the average difference in intensity between a dark and a bright band were less than 30% of the average signal-to-noise level. The important conclusion from this analysis was that the intensity variation over the scanned area was relatively small. The luminescence in the region of the dislocations is modulated by a 15 to 30% change in intensity, but measurable light emission does occur. The dislocation network creates a local variation in charge transport parameters but it is not enough to prevent charge collection when this material is used in detector op-

eration. This result also illustrated the sensitivity of using the direct transport imaging technique to studies defects in semiconductor material.

### *e. Direct Transport Imaging Data with SEM in Spot Mode*

In SEM spot mode, the electron beam is focused at a fixed position on the sample instead of being scanned over a wide area as is done in the previous technique. The direct transport imaging data are obtained by using the CCD camera to image the resulting spatial variation of luminescence intensity. Figure 4-13 illustrates a typical CCD camera image of the direct transport data using SEM in spot mode. The bright spot in the middle of Fig. 4-13a is the luminescence output of the electron beam focused at a point on the InGaAs/GaAs sample. Figure 4-13b displays the intensity profile associated with this spot. (The smaller spot in the image is an artifact created by the secondary reflection of the main spot and the collecting mirror in the optical system.)

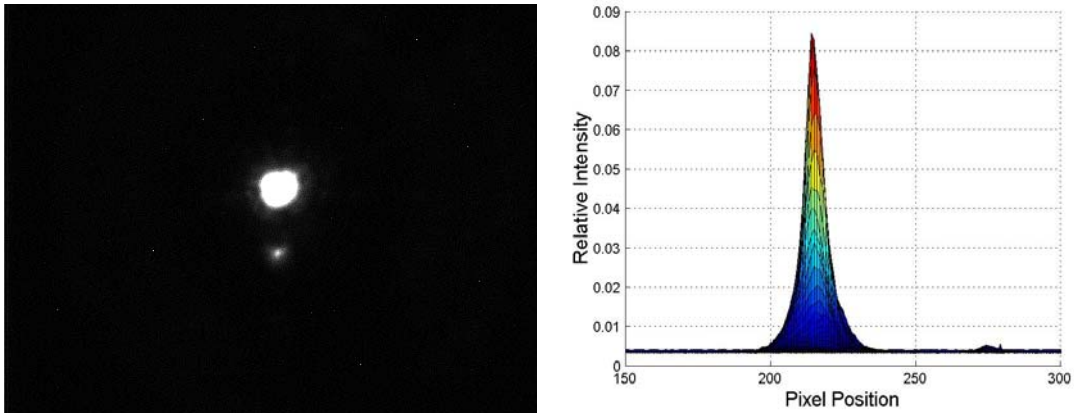


(a) (b)

Fig. 4-13. a) Image of the SEM in spot mode. b) Intensity profile of the same image.

In a typical direct transport imaging study, both drift and diffusion behaviors of free carriers in semiconductor material can be evaluated. Charge diffusion is a direct result of generating free carriers with an electron beam at a point in the material and the creation of a gradient in carrier concentrations. On the other hand, the drift behavior can be observed if an external voltage potential is applied to the sample or if the sample has a build-in internal field (e.g., p-n junction). An electric field forces the free holes and electrons to move along and against the applied field, respectively. The imaging data

would show the drift behavior of the carriers in the bulk material as a function of the applied electric field [3].

The InGaAs/GaAs material used in building the two color IR QWIPs has such a low impedance value (~ 6 ohms at room temperature [1]), so that any applied electric field would have caused an excessively large current to flow in the material. This limits our ability to measure the drift behavior in InGaAs/GaAs QWIPs at room temperature. Nevertheless, we can still apply SEM spot mode to study the diffusion behavior alone without application of any external bias.

One of the problems of using the SEM spot mode to study a non-uniform, dislocations laden area like those of the InGaAs quantum-well layers was the control of the SEM electron beam position. In a spot mode image such as Fig. 4-13a, there was no feedback mechanism to indicate the position of the electron beam with respect to the bright and dark bands as were seen in a scan mode image. An experimental method was developed to locate the beam position in the spot mode with respect to the spatial information of the scan mode data. First, a scan mode of the sample area was acquired. Next, the electron beam control in the SEM was switched to spot mode and the same sample area was obtained. The two images were processed and combined using a routine written in Matlab to adjust for proper image contrast and detail enhancement.

Two case studies of spot mode analysis are presented here. The objective of this analysis is to illustrate the technique described above on two different dislocation regions in the same piece of InGaAs/GaAs sample. Case 1 represented the electron beam positioned over an area where two bright bands intersect. Case 2 was the same study over a dark crossing area. Images were taken with the SEM in scan mode and in spot mode for case 1, as indicated under the column heading of Fig. 4-14. Next, the sample stage was moved so that the electron beam was now focused on the dark crossing of case 2. This was done to assure that all SEM and beam conditions remained constant, while only the material properties were varied. The combined images of scan and spot mode data are shown on the third row of this figure and they illustrate the feedback mechanism needed to precisely control the placement of an electron beam in a non-uniformed sample [10]. The orange lines indicate the targeted position of the electron

| | Case Study 1 | Case Study 2 |
|---|---|---|
| Scan mode | 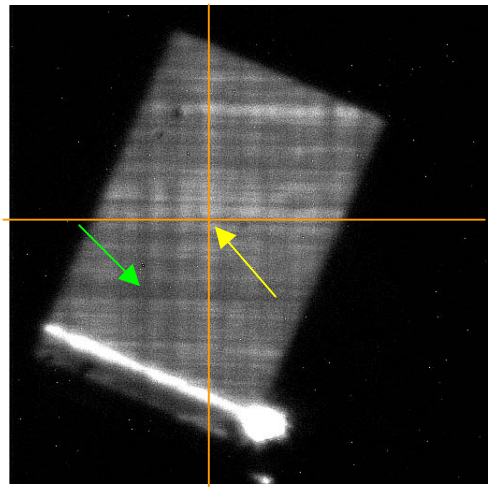 | 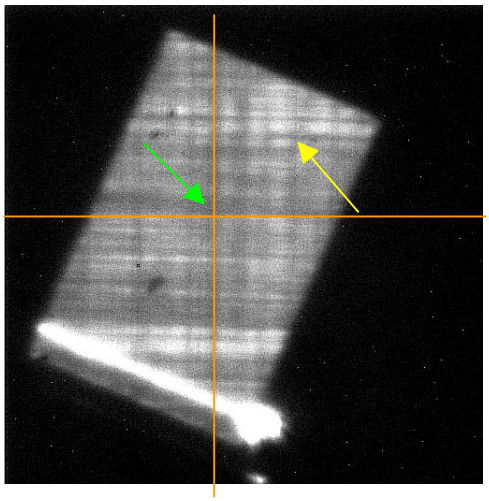 |
| Spot mode | 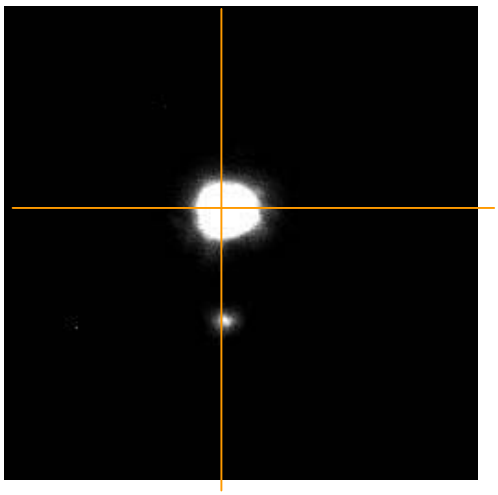 | 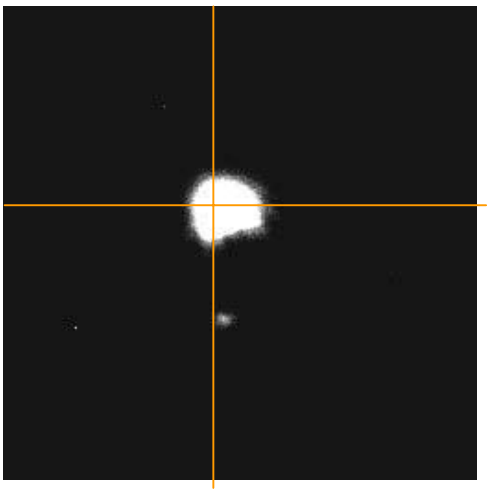 |
| Combined images | 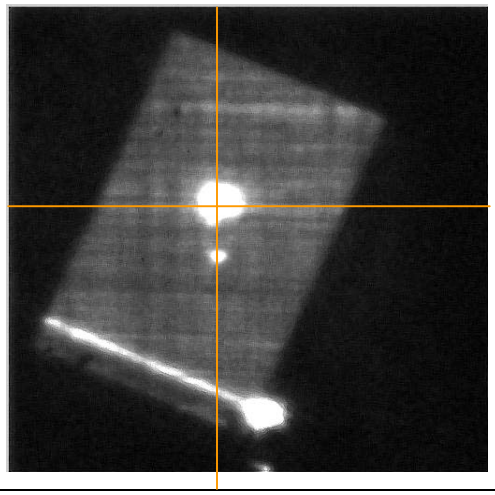 | 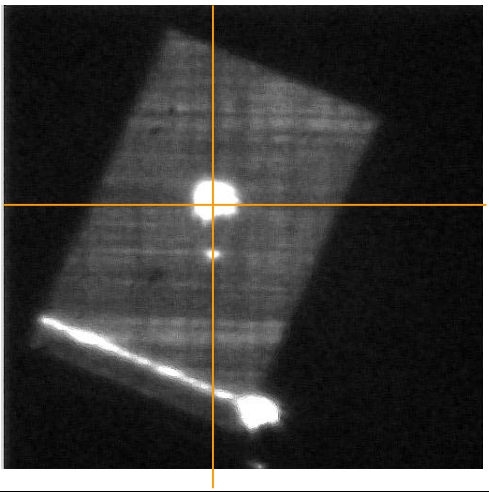 |

Fig. 4-14. Illustration of experimental technique used in studying non-uniform material.

beam in the overall image. The yellow arrows indicate the initial and final position of the bright intersection area as the sample was moved from case 1 to case 2. The green arrows show the same initial and final position of the dark crossing for case 1 and 2.

The overall shape and size of the spot mode images in the second row of Fig. 4-14 looked different from one another and we wanted to analyze this data to see if the differences in the dislocation proximity in these two cases had any effect on the overall intensity response of the material. A close-up view of the raw data revealed differences in peak intensities for each of the two cases so they were normalized to a scale of 0 to 1. Figure 4-15 illustrates a graphical display of the steps involved. After normalization, a cross-sectional area at a constant intensity of 20% of the maximum value was selected from each case to look for changes in total spot area.

| | Case Study 1 | Case Study 2 |
|---|---|---|
| raw data | 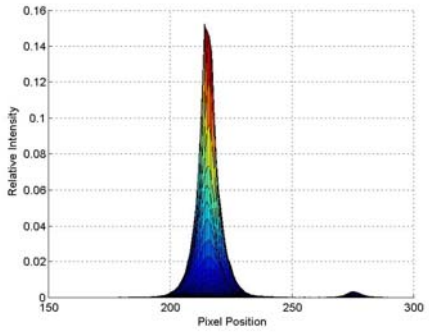 | 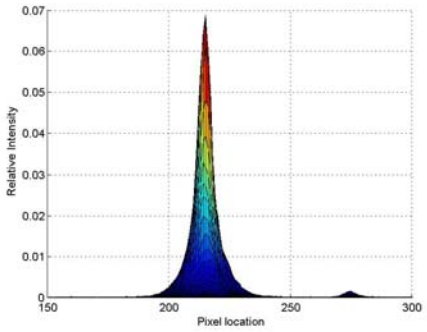 |
| normalized data | 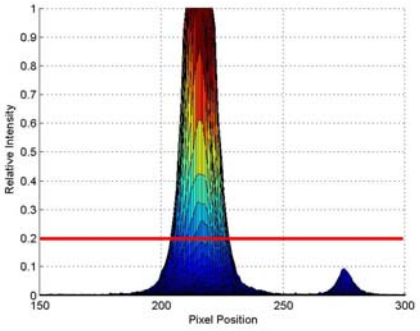 | 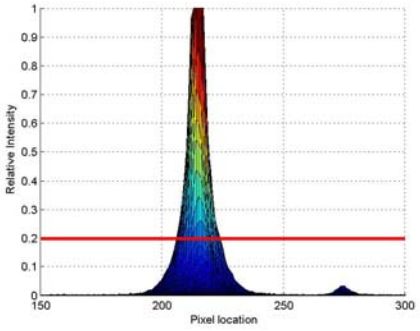 |
| Beam cross-sectional area. | 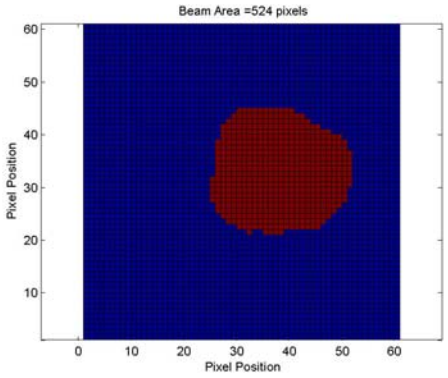 | 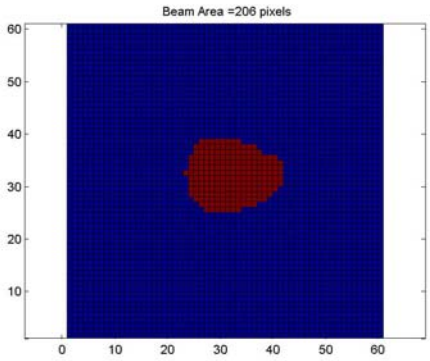 |
| | Area = 513 pixels | Area = 287 pixels |

Fig. 4-15. Matlab analysis of the beam profile in case studies 1 and 2

This meant any pixels with value greater than 0.2 in the normalized image were set to a logical one and the rest were set to a logical zero. The result of this operation was a binary image for each of the two case studies. From these binary images, the area of the beam (in pixels) was obtained for each of the two cases using Matlab routines.

The total cross-sectional area with intensity level higher than 20% in case 1 was measured to be 513 pixels compared to 287 pixels in case 2. This represented an increase in total area of about $(513-287)/287 = 0.7875$ or 78%. The cross-sectional area of the beam at this constant intensity level should have some relationship to the diffusion length property of the material.

The relationship between luminescence radius (hence cross-sectional area) and diffusion length in a material is a topic of ongoing research in this area. Computer simulation of the diffusion of charges in two dimensions shows that the profile will be given by a zero$^{th}$ order modified Bessel function of the second kind [3]. This is plotted in Fig. 4-16 for a range of diffusion length $D^*\tau$. Numerical results indicate that materials with different $D^*\tau$'s will have significant differences in spot size radius at low value (e.g. ~20%) of the normalized peak intensity. The value of 20% of peak intensity in our analysis was chosen so that result can be compared with this numerical simulation.

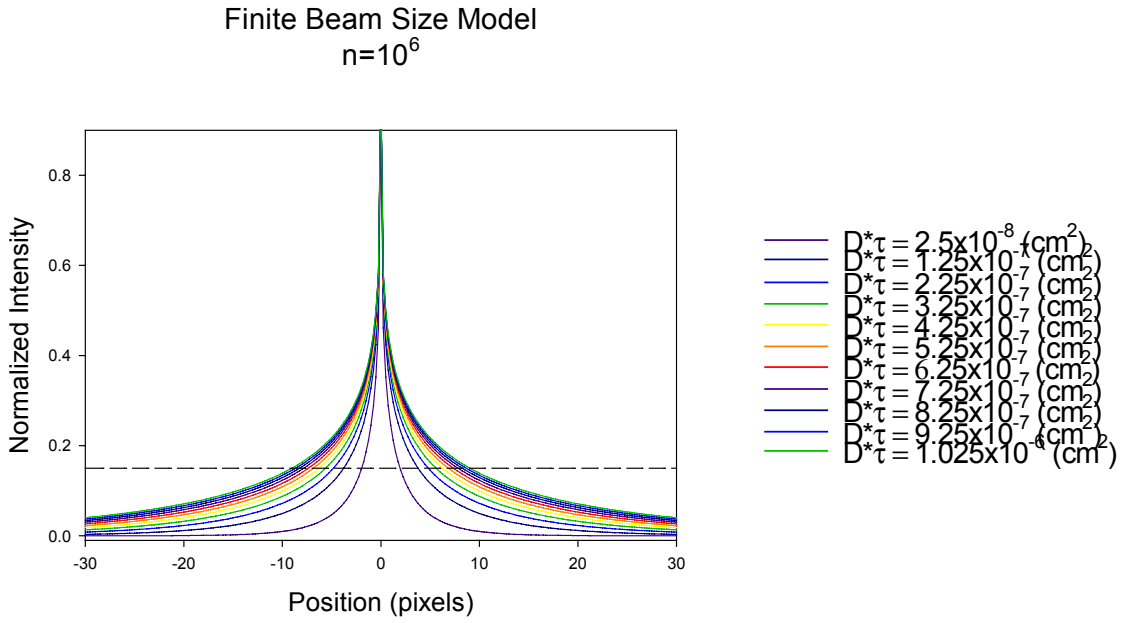


Fig. 4-16. Results from computer simulation of beam size model using Bessel function. (From [15].)

The materials presented in this chapter represent most of the important experimental results gathered with different imaging CL techniques. Edge dislocation patterns were observed in all area of the quantum-well device that contained the InGaAs layer. Further investigation using optical high-pass and low-pass filters were able to confirm that dislocation patterns existed in the InGaAs layer only and that no edge dislocation lines were seen in the cap layer (GaAs). An average dislocation density was measured and so was the amount of intensity fluctuation in the dislocation line. Finally, an initial attempt to use spot mode data to measure variations in diffusion length, $D^*\tau$, for different dislocation pattern was presented. Important scientific results from this investigation will be summarized and presented in the next chapter.

THIS PAGE INTENTIONALLY LEFT BLANK

# V. CONCLUSIONS

The InGaAs/GaAs material system allows for the design of a unique energy band gap structure for two-color quantum-well IR detectors to operate in both the near-IR (1.04 μm) and long-IR (10.6 μm) bands simultaneously. Given the potential role of this type of detector technology in the future target-imaging systems, there is a need to design and optimized these devices and to fully characterize the material properties of InGaAs/-GaAs.

A prototype two-color QWIP was built and demonstrated in laboratory experiment from a previous work [1]. The objective of this thesis was to characterize material properties of the InGaAs/GaAs in a two-color QWIP design in order to relate optical properties to electrical charge transport behavior. Photoluminescence and cathodoluminescence data were collected and analyzed to gauge the material response to external stimulus. A new experimental technique called direct transport imaging was also applied to study dislocation density and diffusion characteristics. The ultimate goal was to extract the pertinent data that could be used for detector's optimization in the next iteration of two-color QWIP design.

Photoluminescence measurements at LBNL and cathodoluminescence studies at NPS were performed to examine material response in the wavelength range from 750 nm to 1800 nm. Response data showed peak emission at 870 and 1019 nm at room temperature, which corresponded to spectral emission from GaAs and InGaAs, respectively. This indicated the material InGaAs/GaAs would be well suited to operate in this spectral region.

A direct transport imaging technique was applied to study the material spatial luminescence response in the Si detection range (400 – 1100 nm). These studies showed an edge dislocation pattern in the area containing InGaAs material. Further studies were able to prove that these patterns were confined only to the active quantum-well layer. The dislocation network created non-radiative recombination centers for free charge in the material. A detector material with very high dislocation density might not perform as well as a

dislocation-free material because the free charges created as the result of interaction with incoming photons can recombine through these dislocations instead of contributing to the desired output photocurrent.

To quantify the effect of these dislocation networks, dislocation density and intensity fluctuation were measured. Using the direct transport imaging technique, dislocation density studies were performed and measured to be about 2000 lines/cm in the InGaAs. The luminescence intensity fluctuation within these networks was also measured to be less than 30% of the signal-to-background intensity level. This fluctuation level should not prevent charge collection in detector operation but an increase in the percentage of Indium in the InGaAs compound may result in higher dislocation density. This might have an adverse affect on the ability of the detector to collect free charge, hence reducing the signal output of the device.

Utilizing the spot mode function of the direct transport imaging technique, a first attempt to measure diffusion length in the InGaAs was made. Initial data showed there was an increase in the overall area of material response from a high-density dislocation region (a dark patch) to a low dislocation region (a bright patch). Although a final diffusion length value was not possible at this stage of the research, the process showed some promise to be used as an important tool to direct measure the diffusion length without first creating external contacts. Future work would include extensive development in data analysis tools to extract the diffusion length, $D^*\tau$, parameter. This would allow a direct comparison between experimental results and those of numerical models.

Clearly, this study of InGaAs/GaAs two-color quantum-well IR photodetectors yields valuable scientific information about the device. Experimental results suggest how to optimize the future's devices for better detection performance. They also demonstrated the potential of charge transport imaging method to relate the spatial luminescence variations observed to charge transport properties that ultimately determine the device's performance.

# LIST OF REFERENCES


1. Touse, Michael P., "Demonstration of a Near and Mid-Infrared Detector Using Multiple Step Quantum Wells", Master's Thesis, Naval Postgraduate School, Monterey, CA, September 2003.

2. Yacobi, B. G. and Holt, D.B., *Cathodoluminescence Microscopy in Inorganic Solids*, Plenum Press, New York, 1990.

3. Haegel, N.M. and Fabbri, J.D. and Coleman, M.P., "Direct Transport Imaging In Planar Structures", *Applied Physics Letters*, **84**, 1329, 2004.

4. Griffiths, David J., *Introduction to Quantum Mechanics*, Prentice Hall Inc., Englewood Cliffs, 1995.

5. Liboff, Richard L., *Introductory Quantum Mechanics, 4$^{th}$ Edition*, Addison Wesley, San Francisco, 2003.

6. Kasap, S. O., *Principles of Electronic Materials and Devices*, McGraw-Hill, New York, 2002.

7. Dereniak, E. L., and Boreman, G. D., *Infrared Detectors and Systems*, John Wiley & Sons, Inc., New York, 1996.

8. Wolfe, William, and Zissis, George J., *The Infrared Handbook*, ERIM, Bellingham, 1993.

9. Haegel, N.M., "Semiconductor Photoconductors for Visible to Far-Infrared Detection", *Photodetectors and Fiber Optics*, Elsevier Science & Technology Books, San Diego, 2001.

10. Smith, Steven W., *Digital Signal Processing*, Elsevier Science & Technology Books, San Diego, 2003.

11. Kasap, S. and Ruda, H., *Illustrated Dictionary of Electronic Materials and Devices*, Concise Student CDROM Edition, S.O. Kasap, New York, 2002.

12. Levine, B.F., "Quantum-well Infrared Photodetectors", *Journal of Applied Physics*, **74**, 1993.

13. Fitzgerald, E.A., Yang, V.K., Ting, S.M, Groenert, M.E., Bulsara, M.T., Currie, M.T., and Leitz, C.W., "Comparison of Luminescent Efficiency of InGaAs Quantum Well Structures", *Journal of Applied Physics*, **93**, 5095, 2003.

14. Gourley, P.L., Fritz, I.J., and Dawson, L.R., "Controversy of Critical Layer Thickness for InGaAs/GaAs Strained-Layer Epitaxy", *Applied Physics Letters*, **52**, 377, 1988.

15. Haegel, N.M., Fabbri, J.D., Hoang, V.D., Freeman, V.W., "Determination of Minority Carrier Diffusion Lengths Through Non-Contact Transport Imaging", in preparation for future publication.

16. Kingfisher International Inc. website. Last accessed 14 June 2004. (http://www.kingfisher.com.au/Finder/DetectorResponse.pdf)

17. Newport Spectra-Physics website. Last accessed 14 June 2004. (http://www.newport.com/store/xq/ASP/lone.Optics/ltwo.Filters+%2526+Attenuators/lthree.Short+and+Long%252DWave+Pass+Filters/lfour./id.3563/isprint./lang.1/qx/productdraw.htm)

# INITIAL DISTRIBUTION LIST

1. Defense Technical Information Center
   Ft. Belvoir, Virginia

2. Dudley Knox Library
   Naval Postgraduate School
   Monterey, California

3. Chairman, Department of Electrical and Computer Engineering, Code EC
   Naval Postgraduate School
   Monterey, California

4. Professor Nancy M. Haegel
   Code PH/35
   Naval Postgraduate School
   Monterey, California

5. Professor John P. Powers
   Code EC/Po
   Naval Postgraduate School
   Monterey, California

6. Professor James H. Luscombe
   Code PH/Lj
   Naval Postgraduate School
   Monterey, California

7. Vu D. Hoang
   412 TW/EWEE
   Edwards AFB, California

8. Oscar L. Alvarado
   412 TW/EWEE
   Edwards AFB, California

9. Peter Burke
   412 TW/EWE
   Edwards AFB, California

10. AFFTC/EWA
    30 Hoglan Ave.
    Bldg. 1030 / Rm 210
    Edwards AFB, California